國立臺灣大學工學院材料科學與工程研究所

碩士論文

Department of Materials Science and Engineering
College of Engineering
National Taiwan University

Master Thesis

導電高分子奈米複合材料塗佈金屬有機骨架薄膜用於太陽能水純化

Metal-Organic Framework (MOF) Based Membranes Coated with Conducting Polymer Nanocomposites for Solar Steam Generation

胡采甯

Tsai-Ning Hu

指導教授：羅世強 博士

Advisor: Shyh-Chyang Luo, Ph.D.

中華民國 111 年 7 月

July, 2022

doi:10.6342/NTU202201614

誌謝

民國 111 年 7 月 19 號，在此我想記錄從沒說出卻真心的感謝。在臺大直升研究所從未是我大學畢業前的計畫，但最後因疫情留下來，我抱持著既來之則安之的想法，而指導教授羅世強老師仍一視同仁的教導我，甚至可說，幸而有羅老師的信任與鼓勵，讓我更喜歡在實驗室做研究，因此改變對未來的規劃。對我來說，羅老師不只是碩士研究上的指導教授更像人生的心靈導師，作為學生的兩年所學遠超過這篇碩士論文的篇幅。同時，幸運的是成為 355 室的一員，在這裡溫暖且和諧，任何實驗和生活的問題都有學長姊及同學的解答和關心。實驗失敗時，總是可以在與大家的討論中摸索失敗原因及改進方向。這裡是我的充電站，更是個不斷吸收、學習的培養皿。謝謝羅老師，謝謝 355 的大家。

和康敦彥老師實驗室的合作，算是在我的碩士研究上天外飛來一筆。康老師嚴格但又充滿心靈雞湯，敦促我在不熟悉的領域中不斷嘗試、進步。各位化工系同學不厭其煩的解答和幫助也對這個研究貢獻匪淺。能藉此機會認識一群這麼優秀又善良的人，再次提醒我是多麼幸運、幸福。謝謝康老師，謝謝化工系的大家。

必須感謝且紀錄的還有我的家人，謝謝每個晚回家的夜晚都有人守門，留下滿桌的飯菜給我；謝謝媽咪每天接我回家，無論多晚多累；謝謝你們讓這個家充滿愛，總是能接住疲倦又挫折的我。

最後，我要謝謝我自己，即使這篇論文還是有所不足及改進空間，但每個寫完論文的研究生都值得掌聲，也值得自己的感謝。

doi:10.6342/NTU202201614

中文摘要

隨著工業的發展和現代科技的進步，世界面臨著水污染和水資源匱乏的問題。近年來，太陽能蒸汽生成、太陽能純化水因其不會額外耗能的優點而備受關注。不同於傳統的淨水方式，其利用太陽能轉化為熱能，通過蒸發後獲得純水，在這個過程中，所有的鹽和雜質都會從蒸汽中分離，蒸汽被冷凝成純水並收集。水純化過程中不會產生污染物、脫鹽膜可以重複使用等優勢，提供了環境友善的水純化方法。純化薄膜或脫鹽膜必須滿足兩項主要性質：1. 可吸收太陽光並轉化成熱能，提供水蒸發的吸收熱。2. 多孔隙、具有連續的微孔結構，提供水分子藉由毛細現象向上傳輸的途徑。另外，熱能須集中在表面，避免熱傳導分散到膜內及底下的水，以達到最高的水蒸發、純化水效率。在此研究中，我們利用三氧化二鈦(Ti_2O_3)及羥基官能化聚(3,4-亞乙基二氧噻吩) (PEDOT-OH)作為光熱轉換材料，並在親水的官能化聚四氟乙烯(polytetrafluoroethylene, PTFE)過濾薄膜上合成原位生長(*in-situ*)的金屬有機骨架(metal-organic framework, MOF) CAU-10-H，藉由 PTFE 基材的孔洞吸收下方的鹽水，再經由 MOF 中的結構孔洞及晶隙傳輸至吸光層，吸收熱能並蒸發。研究中，探討了 PEDOT-OH 和不同比例的 PEDOT-OH 包覆 Ti_2O_3 奈米複合材料的光吸收量及光熱轉換效果，而重量比例 1:1 的 PEDOT-OH 包覆 Ti_2O_3 複合材料能良好塗佈在 MOF 薄膜上又具有最高的吸光量、光熱轉換量。同時，我們合成不同晶體厚度的 *in-situ* CAU-10-H，晶體厚度不但影響水傳輸路徑長短，也會造成絕熱效果的改變。研究結果以厚度 13 μm 的 CAU-10-H 達到兩種機制的平衡，其塗佈薄膜具有最高的水蒸發速率，達 2.17 $kg \cdot m^{-2} \cdot h^{-1}$，而光熱轉換要率達 98%。有別於其他太陽能純化水的發表，緻密 *in-situ* CAU-10-H 的低熱傳導率有利於熱能集中在表面，而此裝置中的脫鹽膜也無須額外的隔熱層以避免熱能分散至水體。結果證明，PEDOT-OH 包覆 Ti_2O_3 奈米複合材料塗佈 CAU-10-H 薄膜在太陽能蒸氣生成及海水淡化等永續能源領域具有巨大的優勢。

關鍵字：導電高分子、金屬有機骨架、太陽純化水。

doi:10.6342/NTU202201614

ABSTRACT

With the advancement of modern technology, the world is facing the issues of water pollution and scarcity of water resources. Solar steam generation and desalination have attracted much attention due to their intrinsic advantages. In the purification process, salts and impurities are separated from the steam, which is condensed into pure water and collected. Moreover, no pollutants are produced during the water purification process. Desalination membranes are also repeatable, providing an environmentally friendly water purification method. In this research, we successfully fabricated titanium trioxide coated with poly(hydroxymethyl EDOT) (Ti_2O_3@PEDOT-OH) nanocomposites as a photothermal conversion material, and well synthesized *in-situ* metal-organic framework (MOF), CAU-10-H based membranes. Ti_2O_3@PEDOT-OH coating 13 μm CAU-10-H self-floating on the water achieves the highest water evaporation rate of 2.17 $kg \cdot m^{-2} \cdot h^{-1}$ with an efficient thermal insulating ability and an evaporation efficiency of 98%. Also, the ion concentrations of collected water tremendously decrease and are much lower than drinkable water standards by WHO. The results have shown that Ti_2O_3@PEDOT-OH nanocomposites on CAU-10-H films possess excellent potential in the fields of sustainable energy such as solar steam generation and seawater desalination.

KEYWORDS: Conducting polymer, PEDOT, metal-organic framework, solar steam generation, solar desalination.

doi:10.6342/NTU202201614

CONTENTS

doi:10.6342/NTU202201614

doi:10.6342/NTU202201614

doi:10.6342/NTU202201614

LIST OF FIGURES

doi:10.6342/NTU202201614

doi:10.6342/NTU202201614

doi:10.6342/NTU202201614

doi:10.6342/NTU202201614

LIST OF TABLES

doi:10.6342/NTU202201614

Chapter 1 Introduction

With the rising human population and the development of industry, the world is facing a scarcity of clean water resources. In order to alleviate water shortage, multiple water treatments, such as seawater desalination and contaminated water purification, captivate global attention to increasing the production of drinkable water. Among all strategies, solar steam generation and solar desalination have attracted exceeding interest from researchers as eco-friendly and sustainable approaches. Different from traditional water purification methods, the energy consumption of the purification process is directly and entirely from solar irradiation. In the desalination process, water evaporates with the heat converted from solar energy. Salts and impurities are separated from the steam, which would be condensed into pure water and collected (**Figure 1-1**[1, 2]). Additionally, no pollutants are produced during the water purification process, and desalination membranes can be repeatably used, thus, providing a green water purification method.

doi:10.6342/NTU202201614

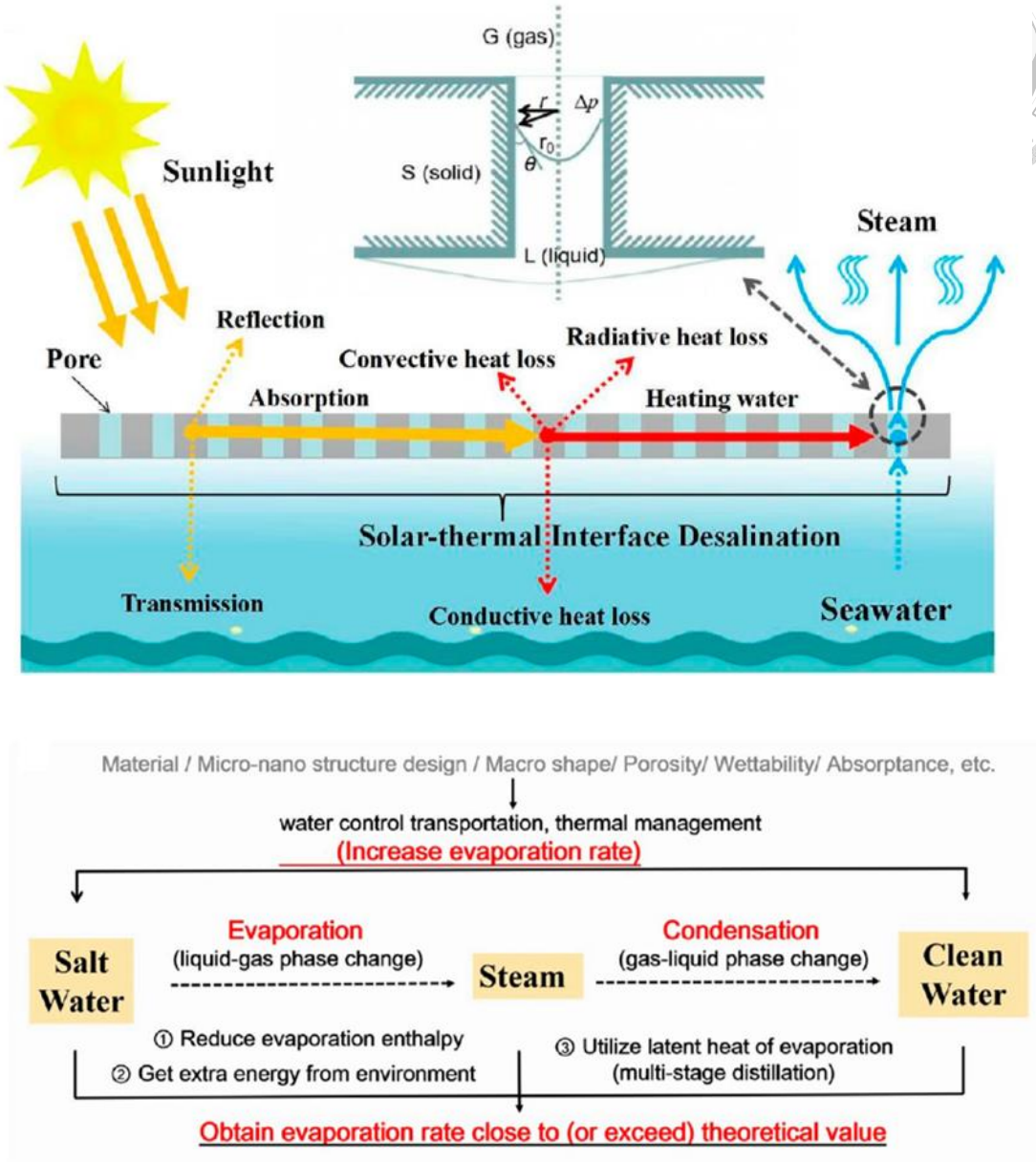

Figure 1-1. Schematic diagram of Mechanism and development [1, 2].

doi:10.6342/NTU202201614

1.1 Desalination Materials

Desalination membranes must hold two main properties: high photothermal capacity and sustainably microporous structure. Solar desalination relies on a photothermal membrane to convert solar energy into heat and provide a localized heated region to make water evaporate.[3] A thermal insulator is usually beneath the desalination membrane in a device to concentrate heat by preventing heat conduction and convection through water molecules to bulk water (**Figure 1-2**).[4, 5] Heat loss also can be diminished with the structure design controlling the pore size of the membranes from nano- to micro-scales.[6-9] Furthermore, consistent pore sizes and sustainable pores are crucial for water permeation. Because water molecules transport upward by a capillary force, the smaller pore sizes can benefit transportation and evaporation rates.

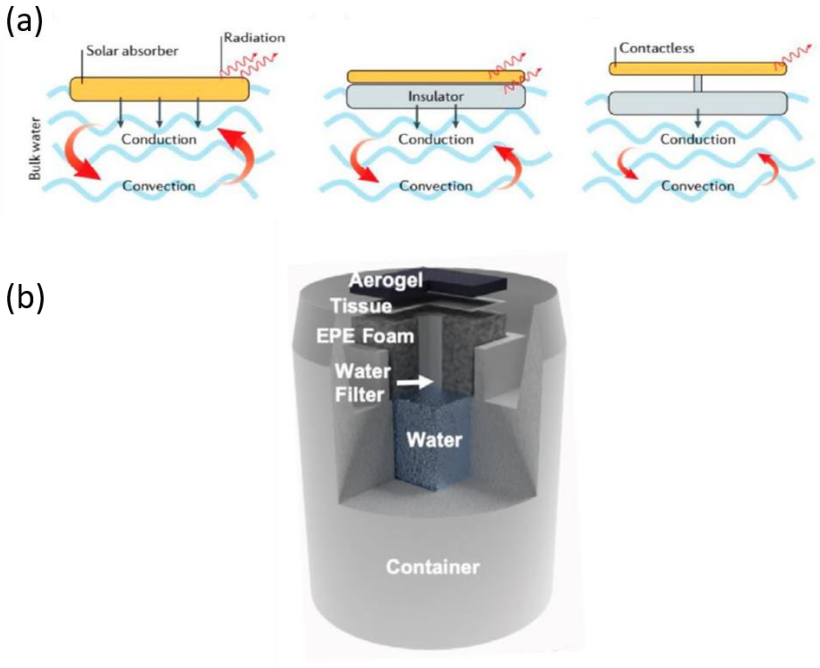

Figure 1-2. (a)The illustration scheme of non-insulator, contact insulator, and contactless insular in solar steam generation devices.[3] (b)The scheme of an actual device with an expanded polyethylene (EPE) foam as a thermal insular and the aerogel as a desalination membrane.[10]

doi:10.6342/NTU202201614

Desalination membranes are often fabricated with hydrogels and aerogels. Hydrogels are 3D polymeric networks with cross-linking. Hydrophilic groups make the high hydrophilicity and high water contents of hydrogels. With a significant amount of water in gels, they can provide an efficient water supply for surface evaporation. The water absorption capacity not only depends on the polar groups of polymer networks but also on the cross-linking density, which further affects the mechanical properties of hydrogels.[11] Moreover, some water molecules form hydrogen bonds with side groups of polymer chains, and thus, present different states of water: bonded water, free water, and intermediate water.[12] The amounts of intermediate water, without intermolecular force, can be tuned with the density of hydrophilic groups to reduce the evaporation enthalpy, and further elevate the evaporation rates.[13-18] However, some problems of hydrogels for solar desalination have not been solved. First, considerable water amount in hydrogels causes heat conduction through water molecules. By reducing the pore sizes with a higher crosslinking density, it is hard to keep the swelling ratio and the density of photothermal composites unchanged.[18] Furthermore, solar absorbers are mostly embedded in hydrogels. The inefficiency of trapping heterogeneous composites eliminates light absorption[19]. Even applying organic absorbers and conducting polymers with physical entanglement or hydrogen bonds to the networks, limited amounts of absorbers lead to low solar absorption. Some of these problems can be solved by aerogels. Aerogels are porous foams with low mass density, including various materials, such as silica, polymer, metal, and carbon. Unlike hydrogels, aerogels lack swelling properties. The hydrophilicity and surface area are tunable through synthesis. Moreover, inorganic absorbers and conducting polymers can be synthesized with chemical bonds to matrix networks. With a more significant amount and higher surface area of light absorbers, the reflection of incident light can be eliminated, and the light

doi:10.6342/NTU202201614

absorption can be elevated.[18, 20-23] In aerogel fabrication, freeze-drying is a common method to achieve a porous structure.[16-18, 20-27] Solar-absorbing composites and crosslinkers are uniformly suspended before freezing and will be well distributed and bonded after annealing.[10, 21] Additionally, freeze-casting is a practical way to acquire vertical channels for water permeation.[20, 25] Despite the improvements of chemically bonded absorbers, aerogels are still facing some issues. Most aerogels have pores larger than submicron scales and large distribution of pore sizes mainly because of the freeze-drying process. Consequently, water permeation is abbreviated, and the heat loss through massive water molecules by conduction, even though aerogels possess low thermal conductivity. Besides, both hydrogels and aerogels cannot directly float on water due to the high water contents in a matrix. It limits device sizes with the need for supporting foams. Therefore, decreasing pore sizes for efficient water permeation, reducing thermal conduction and the weights of wet membranes are critical for further research in solar desalination materials.

1.2 Metal-organic Framework for Solar Desalination

Metal-organic frameworks (MOFs) as crystalline materials have been distinctly focused on due to their high porosity and controllable composition or pore sizes.[28] MOFs are a class of compounds in which metal ions coordinate with organic ligands to form one- to three-dimension structures. The pores in crystal structures can be used as selective material to eliminate guest molecules and filled with particular compounds. Because of this property, MOFs have drawn interest for the storage of gases,[29-35] gas separation,[30, 34-41] water purification,[42-49], and catalysis.[37, 50-53]

For solar desalination, the metal-organic framework has been demonstrated as a

doi:10.6342/NTU202201614

precursor, derived from light-absorbing materials, for example, inorganic materials, such as carbon and metal oxides,[28, 54, 55] or a conducting polymer, polyaniline.[56] Also, the works that copper-based MOFs with high light-absorbing ability have been demonstrated to be promising candidates for solar desalination.[28, 55, 57] Most of the MOF-based desalination membranes were fabricated with metal nanowires, which provides high surface area and the metal elements for further MOF synthesis.[56-58] The crystal of MOFs not only possess additionally surface area but also the surface roughness preventing light reflection and high porosity for water permeation. Moreover, their low thermal conductivity has been proved to benefit heat concentrates on the surfaces[54]. With the abovementioned properties, MOFs are a promising material for desalination membranes and related applications. Thus, we chose Al(OH)(benzene-1,3-dicarboxylate)]·nH2O (CAU-10-H) with high stability in water for desalination membrane synthesis.

1.3 Conducting Polymer Composite as Solar Absorber

Conducting polymers (CPs) were first discovered in the 1970s. The conductivity of CPs is mainly contributed by the delocalized π-bonds and the overlap of π-orbitals on the backbones. With the outstanding properties, such as tunable conductivity,[59, 60] flexibility,[61, 62] and photothermal capacity,[19, 23, 56, 63] conducting polymers have drawn great impacts in the field of science and engineering, and have successfully applied in various applications.

Multiple kinds of CPs have been developed in these few decades, and many of them have been applied as solar absorbers with the photothermal capacity for solar steam generation, for example, polyaniline (PANI) ,[64-69] polypyrrole (PPy) ,[63, 70-74]

doi:10.6342/NTU202201614

poly(3,4-ethylenedioxythiophene) (PEDOT)[75-79]. However, because of the high hydrophobic properties and low water accessibility, beside of combining with other absorbers, polymer mixtures and functionalized conducting polymers commonly facilitates in water remediation and treatments. poly(3,4-ethylenedioxythiophene)-polystyrene sulfonate (PEDOT:PSS), a polymer mixture with hydrophilic polystyrene sulfonate (PSS), is a commercial conducting polymer which can be well suspended in water. It has also been successfully synthesized in aerogels for solar desalination.[10]

In this work, we demonstrate the light absorption and photothermal conversion capacity of hydroxyl functionalized PEDOT (PEDOT-OH) combined with Ti_2O_3. PEDOT-OH shows its high hydrophilicity for water permeation and coating on membranes. Furthermore, its easy nanostructure fabrication benefits light trapping and absorption. The nanocomposites were synthesized with one-step oxidative polymerization. With additional absorption with Ti_2O_3 nanoparticles, Ti_2O_3@PEDOT-OH possesses strong solar absorption capacity across a broad range of wavelengths.

1.4 Research Goal

In this study, we have fabricated Ti_2O_3@PEDOT-OH with different weight ratios and CAU-10-H membranes with different thicknesses. The light absorption and photothermal conversion capacity of Ti_2O_3@PEDOT-OH were measured to find the ratio with the best performances. The thermal insulating abilities of CAU-10-H membranes were also compared and revealed in the work. Finally, evaporation and purification tests were quantified to evidence that the coating CAU-10-H membranes

doi:10.6342/NTU202201614

can be practically applied for solar steam generation and desalination.

doi:10.6342/NTU202201614

Chapter 2 Materials and Methods

2.1 Materials and Instruments

2.1.1 Materials and Chemicals

Table 2-1. The list of chemicals.

Chemicals	Supplier	Purity
Isophthalic acid	Alfa Aesar	99%
Iron(III) chloride	Alfa Aesar	≥99.99%
Aluminum sulfate octadecahydrate	JT Baker	
(2,3-Dihydrothieno(3,4-b)(1,4)dioxin-2-yl)methanol	Sigma-Aldrich	95%
Titanium(III) oxide	Sigma-Aldrich	99.9%

Table 2-2. The list of solvents.

Solvents	Supplier	Purity
N,N-dimethylformamide	Macron	99.8%
Methanol	Macron	99%

Table 2-3. The list of membranes

Membrane	Supplier	Pore Size
Polytetrafluoroethylene membrane filters	Toson Technology	0.1 μm

doi:10.6342/NTU202201614

2.1.2 Instruments and Measurements

Table 2-4. The list of instruments.

Instruments	Supplier
Scanning Electron Microscope	Hitachi S-4800
High Power X-ray Diffractometer	Rigaku TTRAX 3 Rigaku Miniflex
UV-VIS Spectrophotometer	Shimadzu UV-1900i
Xenon light source	Enlitech ALS-300 universal light source
Infrared camera	Testo testo 869,
Contact angle goniometer	Sindatek Model 100 SB
Inductively coupled plasma mass spectrometry	Agilent 7700e

2.2 Nanoparticles and Nanocomposites Fabrication

2.2.1 Ball-milling Process of Ti_2O_3 Nanoparticles

A ball mill (Planetary Mills Ball PM100, Retsch) was utilized in this process with zirconia dioxide balls. The volume fraction of zirconia balls to Ti_2O_3 powder was 30:1. The milling speed was fixed at 300 rpm. In one cycle of the ball milling process, the machine ran continuously for 30 minutes and then stopped for 10 minutes. Tdishe milling time was set to 20 hours. All the procedures are conducted in an argon atmosphere.

doi:10.6342/NTU202201614

2.2.2 Synthesis of PEDOT-OH and Ti_2O_3@PEDOT-OH

The synthesis process is shown in **Figure 2-1.** The synthesis process of PEDOT-OH and Ti_2O_3@PEDOT-OH.. In order to synthesize pure PEDOT-OH and Ti_2O_3@PEDOT-OH with different weight ratios, 500 mg (2.91 mmol) EDOT-OH with none, 150 mg (1.04 mmol), 350 mg (2.44 mmol), 500 mg (3.48 mmol), and 750 mg (5.22 mmol) Ti_2O_3 nanoparticles, respectively, were dissolved and dispersed in 37.5 ml DI water by sonication. The amounts are also shown in **Table 2-5**. The oxidative solution, 2 mmol $FeCl_3$ dissolved in 10 ml DI water, was dripped gently into the stirring PEDOT-OH solution. The mixed solution was stirred at room temperature for 24 h to fully polymerization. After that, the solution was centrifuged and rinsed with DI water to remove the oxidant. This process was repeated four times.

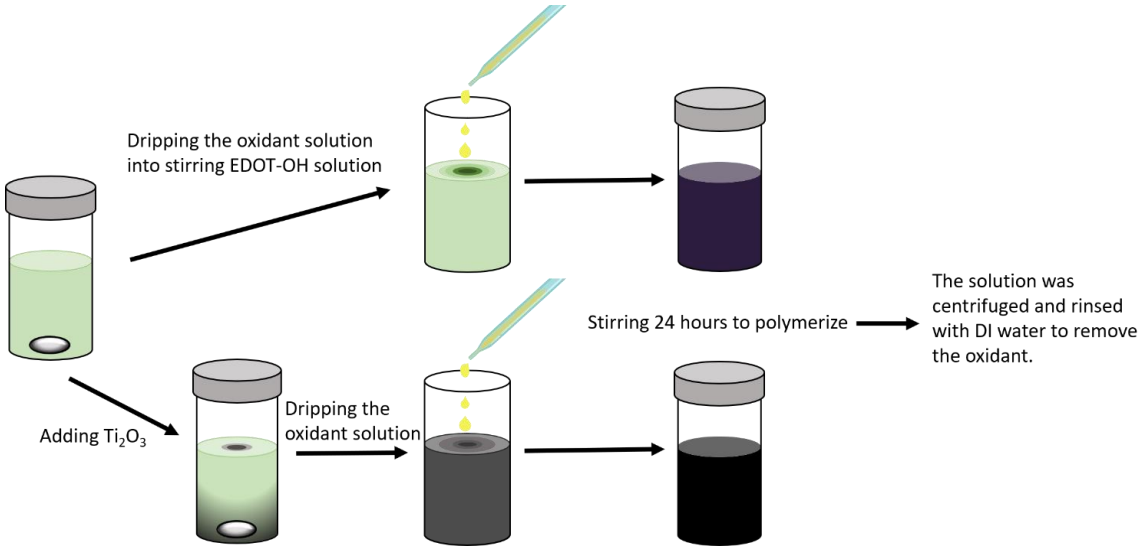

Figure 2-1. The synthesis process of PEDOT-OH and Ti_2O_3@PEDOT-OH.

Table 2-5. The ratios of Ti_2O_3 and EDOT-OH in the synthesis.

Denoting	Ti_2O_3 weight (mg)	Ti_2O_3 mole (mM)	EDOT-OH weight (mg)	EDOT-OH mole (mM)
PEDOT-OH	0	0	500	2.91
0.3_Ti_2O_3@PEDOT-OH	150	1.04	500	2.91

doi:10.6342/NTU202201614

0.7_Ti_2O_3@PEDOT-OH	350	2.44	500	2.91
1.0_Ti_2O_3@PEDOT-OH	500	3.48	500	2.91
1.5_Ti_2O_3@PEDOT-OH	750	5.22	500	2.91

2.3 Synthesis of CAU-10-H

2.3.1 Synthesis of CAU-10-H in Powder Form

5 mmol $Al_2(SO_4)_3 \cdot 18H_2O$ and 5 mmol 1,3-H_2BTC were dissolved in a cosolvent of 24 ml distilled water and 6 ml DMF. The solution was stirred at a refluxed temperature of 120 ^oC for 48 hours. After synthesizing, the CAU-10-H powder was collected by vacuum filtration, rinsed with DI water, and then dried in the oven at 100 ^oC for 24 hours to remove the solvents.

2.3.2 Synthesis of *in-situ* CAU-10-H Membranes

0.2 wt% CAU-10-H powder was sonicated and dispersed in distilled water as a seeding solution. The solution was dripped to cover the PTFE substrates and spin-coated at 1000 rpm for 30 seconds. The substrates were baked to dry in the oven at 50 ^oC for 20 minutes. This process was repeated three times for powder seeding. The details of reactants, solvents, and temperatures are shown in **Table 2-5.** For 7 μm thick CAU-10-H membrane, the seeded substrate was immersed in the secondary growth solution, prepared with 2.5 mmol $Al_2(SO_4)_3 \cdot 18H_2O$ and 2.5 mmol 1,3-H_2BTC in 144 ml distilled water and 36 ml DMF cosolvent. For a 10 μm thick CAU-10-H membrane, the seeded substrate was immersed in the secondary growth solution, prepared with 5 mmol $Al_2(SO_4)_3 \cdot 18H_2O$ and 5 mmol 1,3-H_2BTC in a cosolvent of 144 ml distilled water and 44 ml DMF cosolvent. For a 13 μm thick CAU-10-H membrane, the seeded substrate was immersed in the secondary growth solution, prepared with 2.5 mmol $Al_2(SO_4)_3 \cdot 18H_2O$ and 2.5 mmol 1,3-H_2BTC in a cosolvent of 144 ml distilled water and 36 ml DMF. For a 15 μm thick CAU-10-H membrane, the seeded substrate was

doi:10.6342/NTU202201614

immersed in the secondary growth solution, prepared with 5 mmol $Al_2(SO_4)_3 \cdot 18H_2O$ and 5 mmol in a cosolvent of 1,3-H_2BTC in 144 ml distilled water and 36 ml DMF. For a 17 μm thick CAU-10-H membrane, the seeded substrate was immersed in the secondary growth solution, prepared with 5 mmol $Al_2(SO_4)_3 \cdot 18H_2O$ and 5 mmol 1,3-H_2BTC in a cosolvent of 144 ml distilled water and 44 ml DMF. The reaction was at a refluxed temperature of 110 ºC for 24 hours. After that, the substrate was rinsed with distilled water to remove deposited particles and then immersed in the new secondary-growth solution for continuous growth at the same condition. After synthesizing, CAU-10-H membranes were activated by thoroughly soaking in methanol for 24 hours. Finally, the membranes were dried in the oven at 50 ºC for 24 hours to remove methanol.

Table 2-6. The reactant quantities and methods of CAU-10-H membranes with different thicknesses.

	Synthesis method	**$Al_2(SO_4)_3 \cdot 18H_2O$ (mmol)**	**1,3-H_2BTC (mmol)**	**DMF (ml)**	**DI water (ml)**	**Temperature (ºC)**
7 μm CAU-10-H	2nd growth	2.5	2.5	36	144	100
10 μm CAU-10-H	2nd growth	5	5	44	144	110
13 μm CAU-10-H	3rd growth	2.5	2.5	36	144	100
15 μm CAU-10-H	3rd growth	5	5	36	144	100
17 μm CAU-10-H	3rd growth	5	5	44	144	110

2.4 Coating Composites on CAU-10-H Membranes

15 wt % PEDOT-OH or Ti_2O_3@PEDOT-OH was dispersed in DI water by

doi:10.6342/NTU202201614

sonication. 0.2 ml/cm^2 dispersion solution was dripped on CAU-10-H membranes and dried on a hotplate at 60 ^{o}C.

2.5 Characterization

2.5.1 Scanning Electron Microscope (SEM)

The morphologies and microstructures of all membranes were determined by SEM. A Hitachi S-4800 field emission SEM was used with an acceleration voltage of 10 kV. Every sample has been coated with platinum via sputter deposition with an acceleration voltage of 25 V for 40 seconds.

2.5.2 UV-VIS Spectrophotometer

The absorption spectra of all composites were characterized by an ultraviolet-visible spectrophotometer (UV-1900i, Shimadzu). The measurements were conducted from 1100 nm to 250 nm with a 13 nm per second scan rate, and 0.7 wt % dispersion solutions were prepared for measurements.

2.5.3 Contact Angle Measurements

The hydrophilicity and water-absorbing effects of surfaces were demonstrated with contact angle measurements. A contact angle goniometer (Model 100 SB, Sindatek) was utilized in the experiments. The needle squeezed a drop of DI water, and the platform was elevated to drip DI water on the surfaces of the samples. The images were captured to measure the contact angles.

2.5.4 X-ray Powder Diffraction (XRD)

High Power X-ray Diffractometer (TTRAX 3, Rigaku) was utilized with Cu Kα radiation (50 kV, 300 mA). Each sample was scanned from 5^o to 65^o 2θ with a step size of 0.02^o 2θ using an incident beam of 0^o.

doi:10.6342/NTU202201614

2.5.5 X-ray Diffraction (XRD)

X-ray Diffractometer (MiniFlex, Rigaku) was utilized for crystal analysis of membranes, conducted with Cu Kα (50 kV, 300 mA). Each XRD result was scanned from 5° to 28° 2θ with a step size of 0.01° 2θ using an incident beam of 1°.

2.5.6 Inductively Coupled Plasma Mass Spectrometry (ICP-MS)

The ion concentrations were analyzed with ICP-MS (7700e, Agilent) including elements of Na, K, Ca, and Mg.

2.6 Evaporation and Purification Tests

2.6.1 Device Setup of Evaporation Tests

As **Figure 2-2** shown, the device setup includes a solar simulator, an electronic balance, an IR camera, and the desalination device to measure instant temperatures and weight loss for calculating evaporation rates.

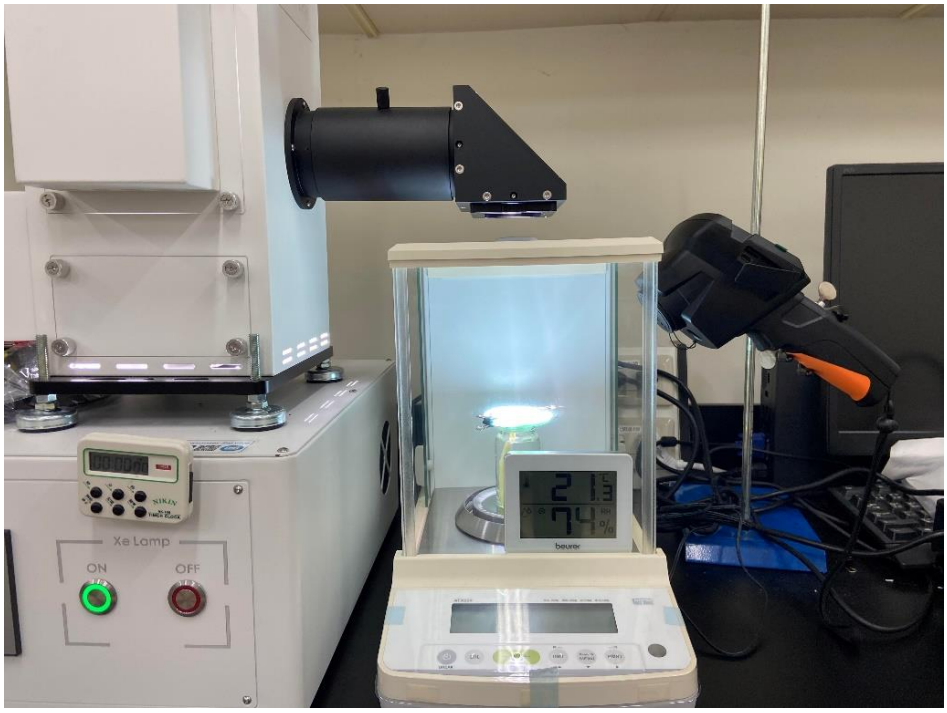

Figure 2-2. The photo of the device setup for evaporation tests. The desalination device

doi:10.6342/NTU202201614

was placed in an electronic balance to measure weight loss under the xenon lamp as a solar simulator, and an IR camera was fixed to measure the temperatures of a fixed point on membrane surfaces.

Two different desalination devices are shown in **Figure 2-3. Figure 2-3a** shows a 3D printing device to isolate the desalination membrane from bulk water, and **Figure 2-3b** shows the desalination membrane floating on bulk water. Two devices are constructed to compare the thermal insulating ability of *in-situ* CAU-10-H membranes.

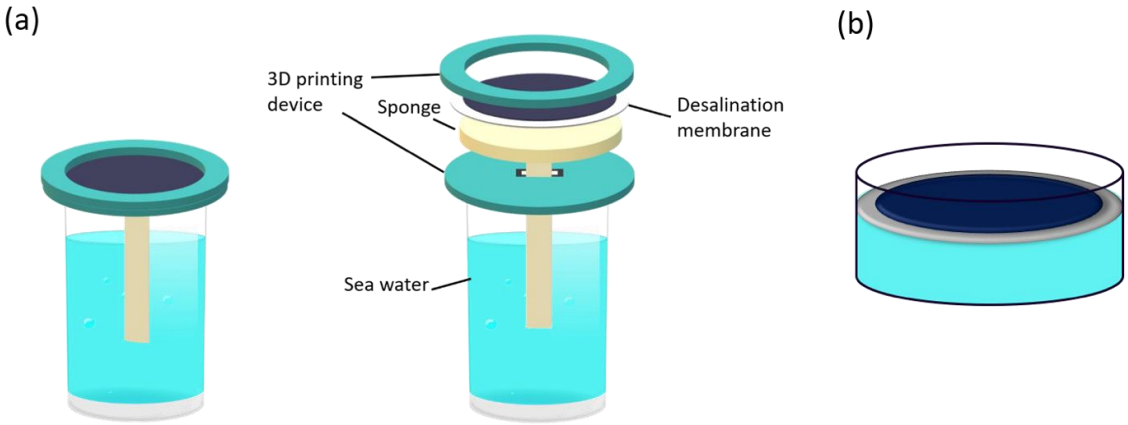

Figure 2-3. (a) The 3D printing device to clamp the desalination membrane and a sponge which is for water absorption and separate the desalination membrane and simulated seawater. (b) The scheme of the desalination membrane directly floating on simulated seawater.

2.6.2 Device to Collect Condensed Water

The purification device is for collecting pure water. The actual device and the illustration of purification process are shown in **Figure 2-4**

doi:10.6342/NTU202201614

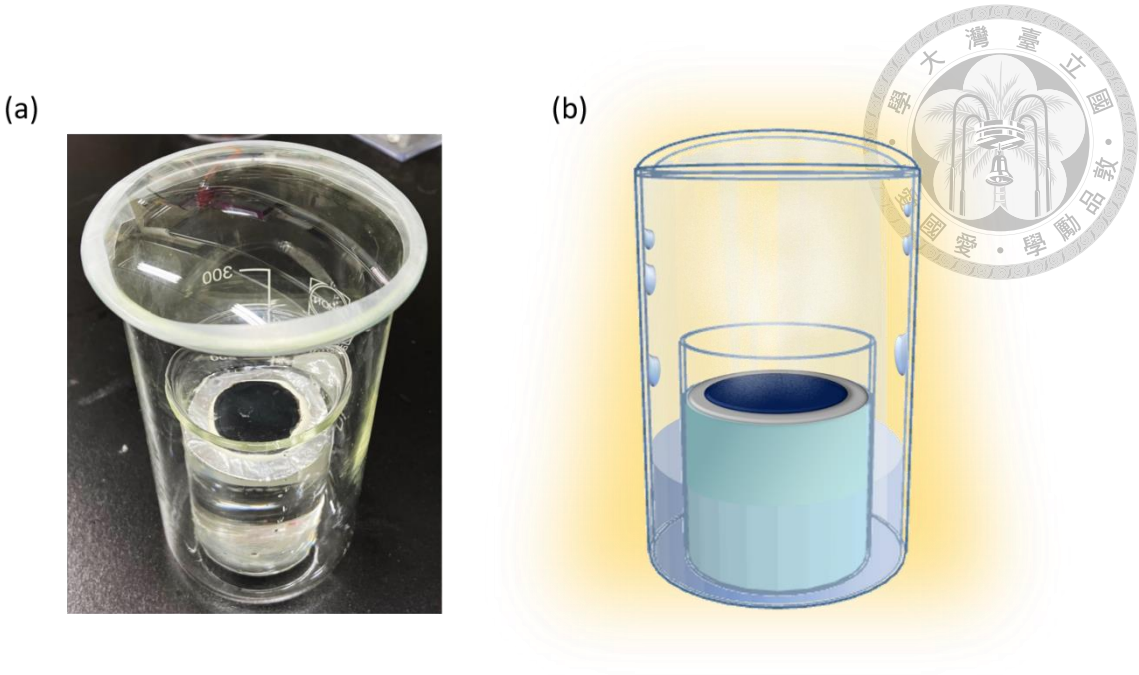

Figure 2-4. (a) The device condensing pore water. (b) The illustration of the device to collect condensed water. Under solar illumination, the membrane converts irradiation to heat to make water evaporates and condenses along the glass.

doi:10.6342/NTU202201614

Chapter 3 Result and Discussion

3.1 Photothermal Composites

3.1.1 Comparison between PEDOT-OH and Ti_2O_3@PEDOT-OH

Light absorption capacity is essential for solar steam generation. To demonstrate high light absorption in a broad range of wavelengths, Ti_2O_3 nanoparticles are added to PEDOT-OH polymerization to acquire Ti_2O_3-coated PEDOT-OH. Pure Ti_2O_3 nanoparticles are also widely used as solar absorbers due to their high light-absorbing capacity in a wide wavelength range. However, they are hardly coated on films and substrates without surfactants. Worth noting that because of oxygen vacancy on the Ti_2O_3 particle surface, Ti_2O_3 particles can be well dispersed by hydroxyl groups of PEDOT-OH in deionized water and coated on *in-situ* CAU-10-H without additional surfactants.[80] The UV/VIS absorption spectrums of PEDOT-OH, Ti_2O_3, and Ti_2O_3@PEDOT-OH were conducted by a UV/VIS spectrophotometer (**Figure 3-1a)**. The measurements were performed from 1100 nm to 250 nm with a 13 nm per second scan rate, and 0.7 wt % suspension solutions were prepared for measurements. The spectrum Ti_2O_3@PEDOT-OH shows increasing absorption in the wavelengths below 600 nm because of the absorption of Ti_2O_3 particles. The peaks at 250 nm and 310 nm in the Ti_2O_3@PEDOT-OH spectrum might be O-H absorption enhanced by the interaction between hydroxyl groups of PEDOT-OH and Ti_2O_3. **Figure 3-1b** shows evaporation rates of CAU-10-H with different coatings. Pure CAU-10-H without photothermal absorbers shows the lowest rate. Ti_2O_3@PEDOT-OH coating membrane possesses the highest rate, slightly above the PEDOT-OH coating membrane. It further confirms that adding Ti_2O_3 particles can improve the light absorption ability,

doi:10.6342/NTU202201614

photothermal capacity, and consequently evaporation rates, and Ti_2O_3@PEDOT-OH can be an efficient solar absorber.

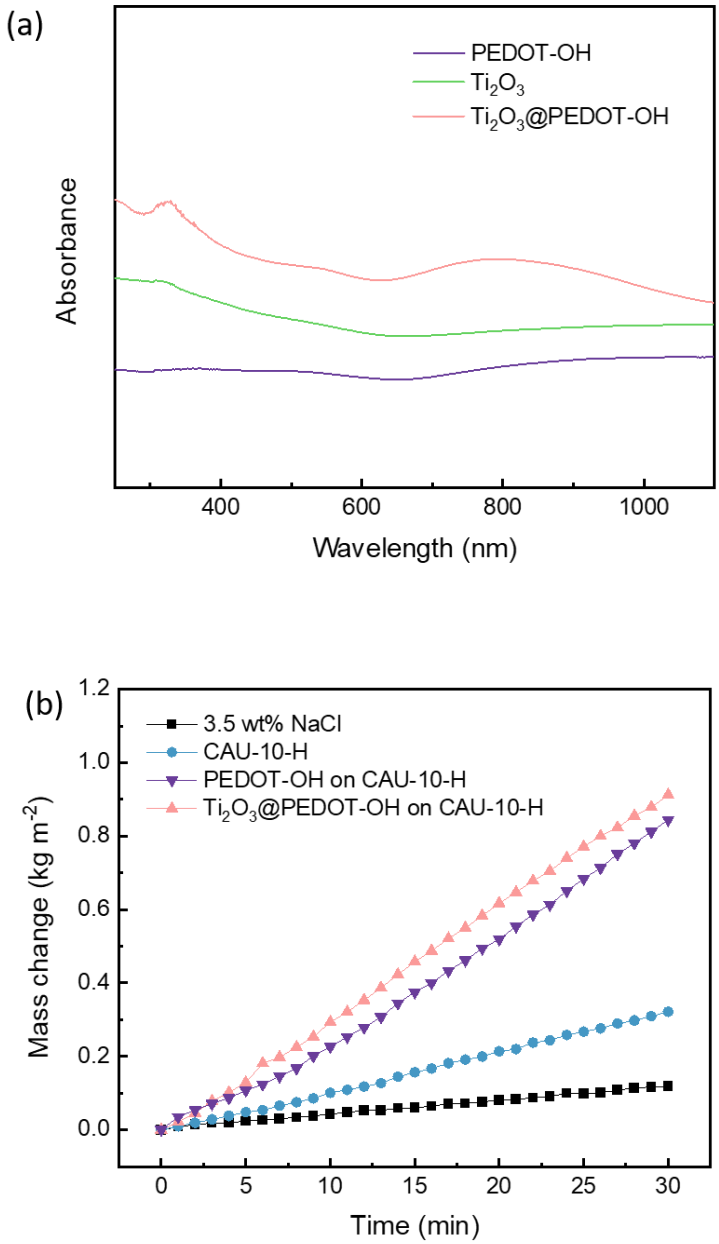

Figure 3-1. (a) UV/VIS absorption spectrum of PEDOT-OH, Ti_2O_3, and as-received Ti_2O_3@PEDOT-OH. (b) Evaporation rates of PEDOT-OH and as-received Ti_2O_3@PEDOT-OH coating on CAU-10-H membranes.

doi:10.6342/NTU202201614

3.1.2 Comparison between As-received Ti_2O_3 and Ti_2O_3 Nanoparticles

Ti_2O_3 nanoparticles were obtained with the ball-mill process to eliminate light reflection. After ball-milling, XRD results confirmed that no oxidation occurs in this process (**Figure 3-2**). The characteristic peaks of Ti_2O_3 nanoparticles are fitted with as-received Ti_2O_3 but broader because of the stress-strain field from the ball-milling. Moreover, in the SEM images, the particle sizes become averaged and decrease from micrometers to about one hundred nanometers (**Figure 3-3**). The light absorptions of as-received Ti_2O_3@PEDOT-OH and Ti_2O_3 nanoparticle@PEDOT-OH (nanoTi_2O_3@PEDOT-OH) are also demonstrated (**Figure 3-4a**). It shows that the two characteristic spectrums are almost the same, and the absorptivity of nanoTi_2O_3@PEDOT-OH is much higher than the other. **Figure 3-4b** shows the temperature changes of different coatings. The temperature of nanoTi_2O_3@PEDOT-OH is slightly higher than Ti_2O_3@PEDOT-OH, specifying that reducing particle sizes can efficiently intensify photothermal capacity.

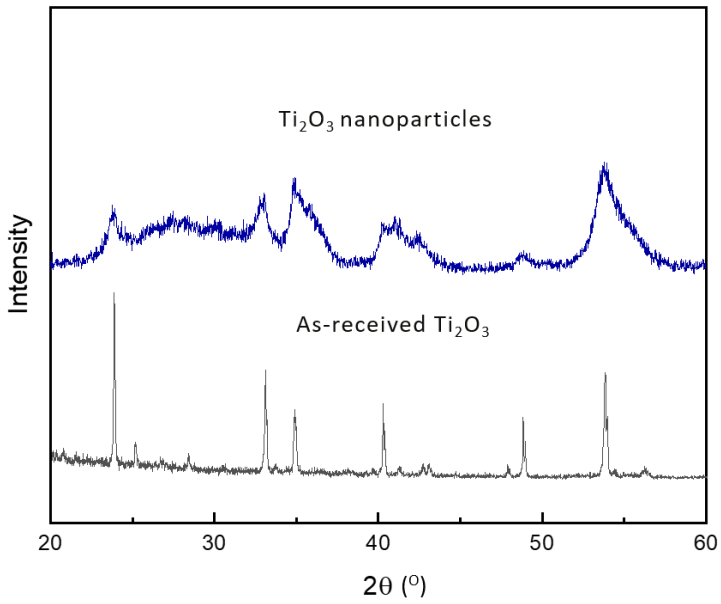

Figure 3-2. XRD results of as-received Ti_2O_3 and Ti_2O_3 nanoparticles after ball-milled.

doi:10.6342/NTU202201614

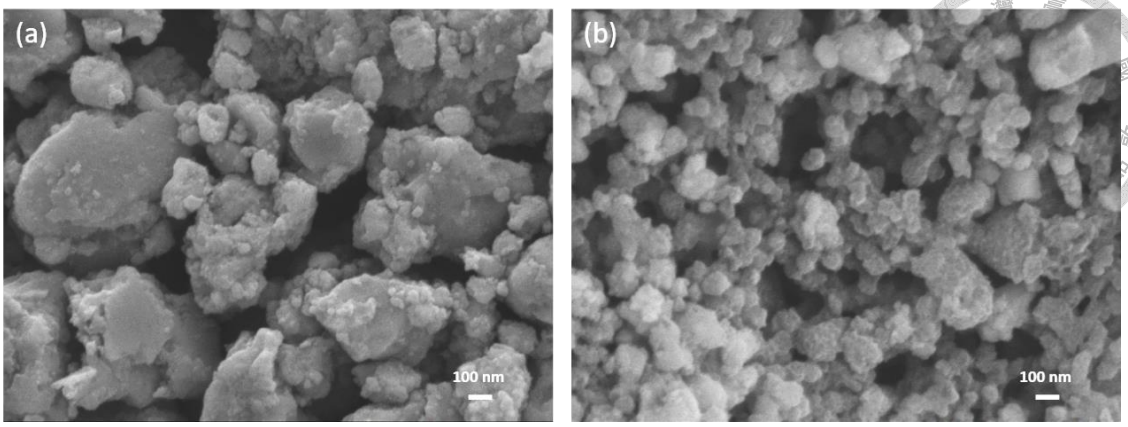

Figure 3-3. SEM results of (a) As-received Ti_2O_3@PEDOT-OH. (b) nanoTi_2O_3@PEDOT-OH

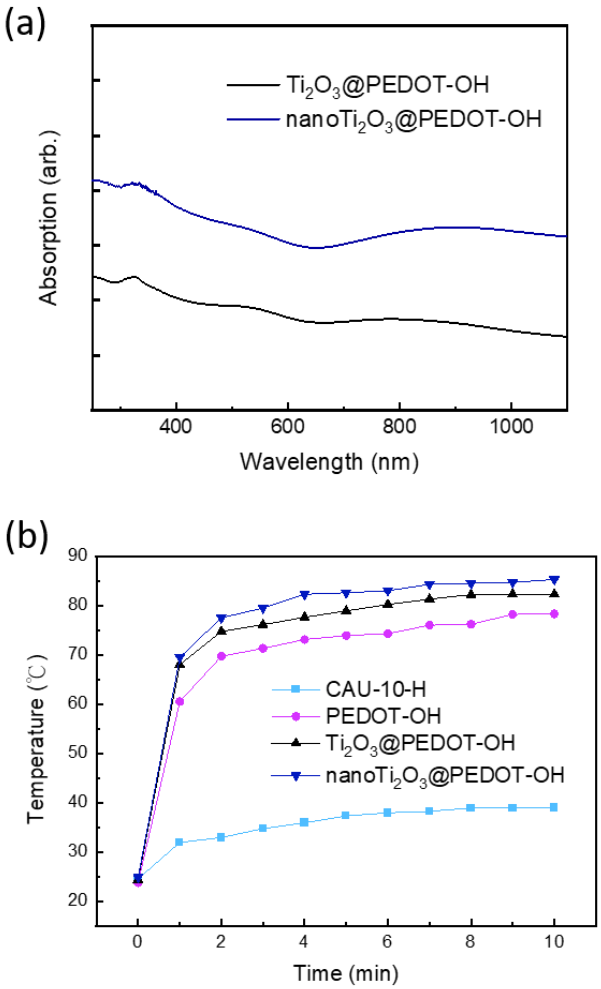

Figure 3-4. (a) Light absorption of as-received Ti_2O_3@PEDOT-OH and nanoTi_2O_3@PEDOT-OH. (b)Temperatures of different coatings in a dry state.

doi:10.6342/NTU202201614

3.1.3 Ti_2O_3@PEDOT-OH Nanocomposites with Different Ratios

To compare the absorptivity, the absorption spectra of pure PEDOT-OH and nanocomposites with different weight ratios, denoted as 0.3_Ti_2O_3@PEDOT-OH, 0.7_Ti_2O_3@PEDOT-OH, 1.0_Ti_2O_3@PEDOT-OH, and 1.5_Ti_2O_3@PEDOT-OH, were characterized by a UV-VIS spectrophotometer. From the spectrum, the light absorption enhances as the ratio of Ti_2O_3 nanoparticles increases (**Figure 3-5a**). However, when the proportion of Ti_2O_3 is too massive, some nanoparticles cannot be well dispersed with hydroxyl groups of PEDOT-OH and would agglomerate in DI water. Therefore, in the spectrum of 1.5_Ti_2O_3@PEDOT-OH, the absorbance decreases over time, indicating the deposition of nanocomposites.

To estimate solar-to-thermal conversion ability, nanocomposites were coated on PTFE substrates to measure temperature changes in a dry state with an infrared camera (**Figure 3-5b**, **Figure 3-6**). A xenon light source was used as a solar simulator. Under exposure to one-sun illumination, temperatures of all coated substrates rise significantly in the first minutes and keep slightly rising for the rest of the time. From pure PEDOT-OH to 1.5_Ti_2O_3@PEDOT-OH, the maximum temperatures of each coating are 67.5 ^oC, 71.5 ^oC, 74.4 ^oC, 77.4 ^oC, and 78.4 ^oC, respectively. The temperature result follows the same trend as the UV-VIS result and the increasing ratio of Ti_2O_3 over PEDOT-OH. It presents that 1.5_Ti_2O_3@PEDOT-OH coating possesses the highest temperature and PEDOT-OH coating possesses the lowest temperature.

Temperature changes in a wet state are also presented in **Figure 3-5c** and **Figure 3-7**. Furthermore, the evaporation rates are also exhibited in **Figure 3-8** and **Table 3-1**. The maximum temperatures of different coating still hold the same trend. On the other hand, the temperature deviation of different coatings in a wet state is smaller than in a

doi:10.6342/NTU202201614

dry state because the heat conducts and loss through water molecules. The contrast indicates, compared to solar-to-thermal conversion capacity, thermal insulating ability of membranes is also important to maintain high photothermal capacity on the surfaces for water evaporation. Moreover, the wet temperatures directly affect the evaporation rates. The evaporation rates of different coatings on PTFE substrates also possess slight variation. 0.3_Ti_2O_3@PEDOT-OH and 0.7_Ti_2O_3@PEDOT-OH coating possess nearly the same rates. The rates of 1.0_Ti_2O_3@PEDOT-OH and 1.5_Ti_2O_3@PEDOT-OH coating substrates enhance respectively as the same trend above. However, because of the aggregation of Ti_2O_3 mentioned above, 1.5_Ti_2O_3@PEDOT-OH cannot be sustainable coated on *in-situ* CAU-10-H. Therefore, 1.0_Ti_2O_3@PEDOT-OH would be the best candidate as a solar absorbing layer and further used as a solar absorbing coating in later experiments and results.

doi:10.6342/NTU202201614

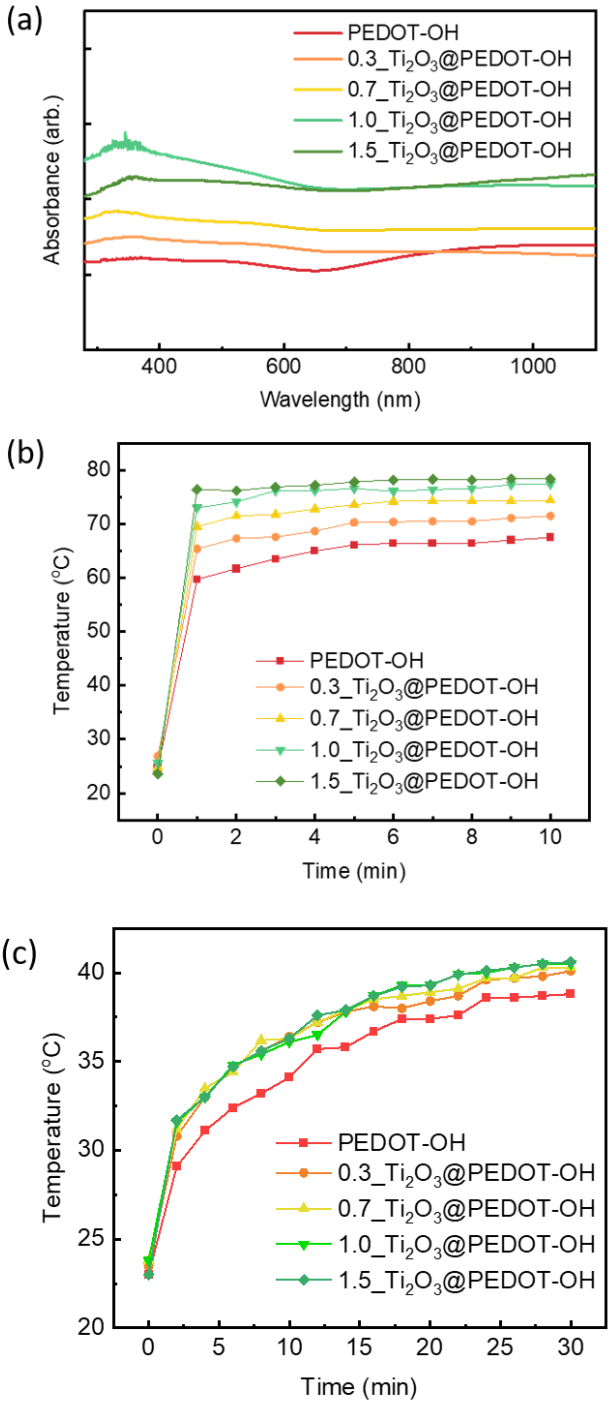

Figure 3-5. (a) UV-vis-NIR spectrum of PEDOT-OH and Ti_2O_3@PEDOT-OH nanocomposites with different ratios. 0.7 wt % nanocomposites were dispersed in DI water after ultrasonication. (b) Temperatures at a dry state of PEDOT-OH and Ti_2O_3@PEDOT-OH nanocomposites with different ratios coating on PTFE substrates under one sun illumination. (c) Temperatures at a wet state.

doi:10.6342/NTU202201614

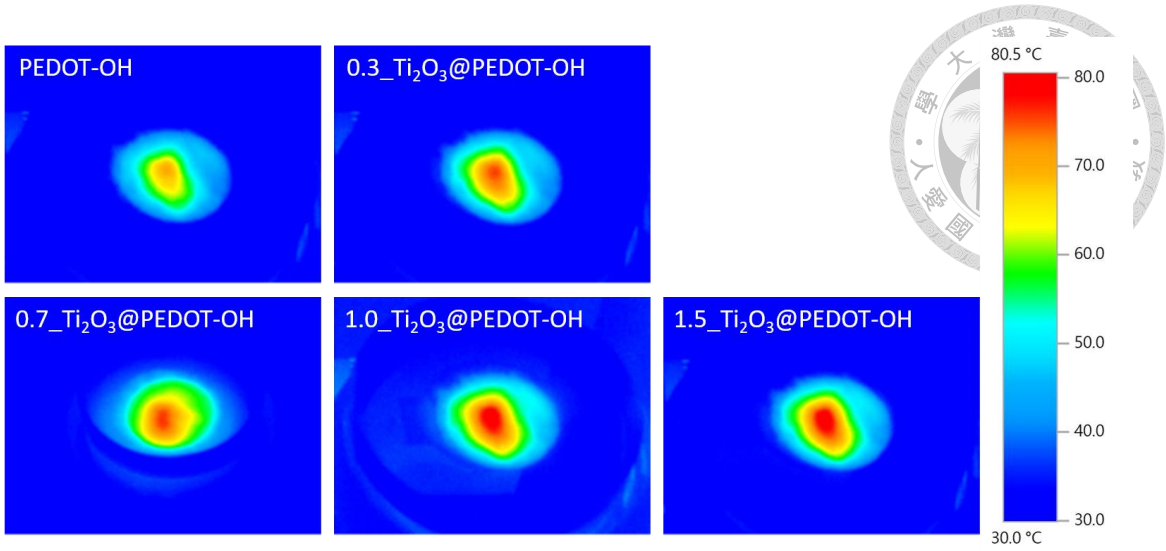

Figure 3-6. IR images of different coatings on PTFE substrates in a dry state after ten minutes of one-sun irradiation.

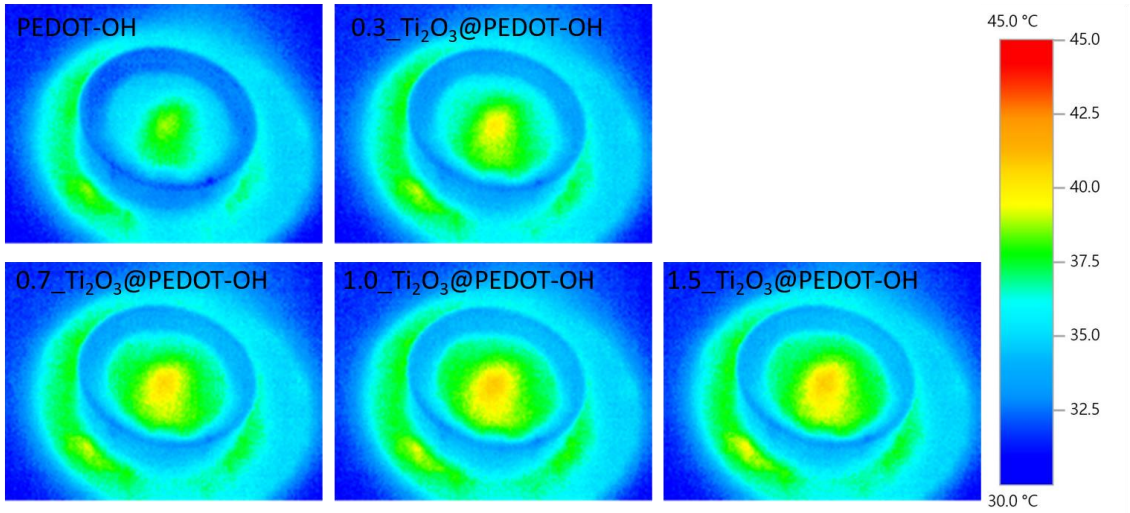

Figure 3-7. IR images of different coatings on PTFE substrates in a wet state after thirty minutes of one-sun irradiation.

doi:10.6342/NTU202201614

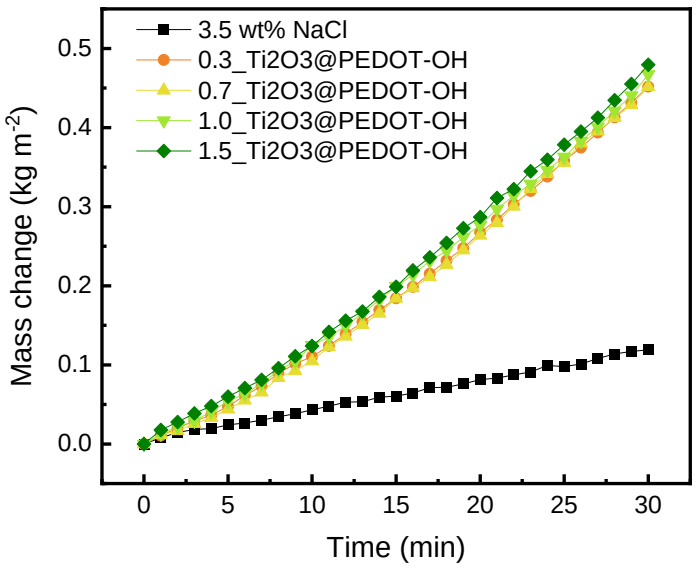

Figure 3-8. Evaporation rates of different coatings on PTFE substrates.

Table 3-1. Evaporation rates of different coatings on PTFE substrates.

Coating	**Evaporation rate ($kg \cdot h^{-1} \cdot m^{-2}$)**
0.3_Ti_2O_3@PEDOT-OH	0.903
0.7_Ti_2O_3@PEDOT-OH	0.903
1.0_Ti_2O_3@PEDOT-OH	0.934
1.5_Ti_2O_3@PEDOT-OH	0.959

doi:10.6342/NTU202201614

3.1.4 The Dispersity of Nanocomposites

To further reveal the dispersity of different nanocomposites, 4 wt % suspension aqueous solutions were prepared and placed still as **Figure 3-9**. After two hours, 1.5_Ti_2O_3@PEDOT-OH nanocomposites with the highest amount of Ti_2O_3 almost fully precipitate. After four hours, the top of 0.7_Ti_2O_3@PEDOT-OH and 1.0_Ti_2O_3@PEDOT-OH solutions became transparent compared to the two-hour image, and PEDOT-OH solution was still well dispersed without deposition. After twenty-four hours, all vials with nanocomposites presented deposition. 1.5_Ti_2O_3@PEDOT-OH solution with black residues at the bottom was transparent and pure. Additionally, 0.7_Ti_2O_3@PEDOT-OH and 1.0_Ti_2O_3@PEDOT-OH solutions also presented black residues but with darker solutions and fewer deposition, and because of the higher amount of PEDOT-OH, 0.7_Ti_2O_3@PEDOT-OH showed deep purple in the solution. On the other hand, only the top of PEDOT-OH suspension solution showed transparency and most of solution kept dark without obvious deposition. Thus, these images reveal that the dispersity drops when the amount of Ti_2O_3 nanoparticles increases, as previous observation shows.

doi:10.6342/NTU202201614

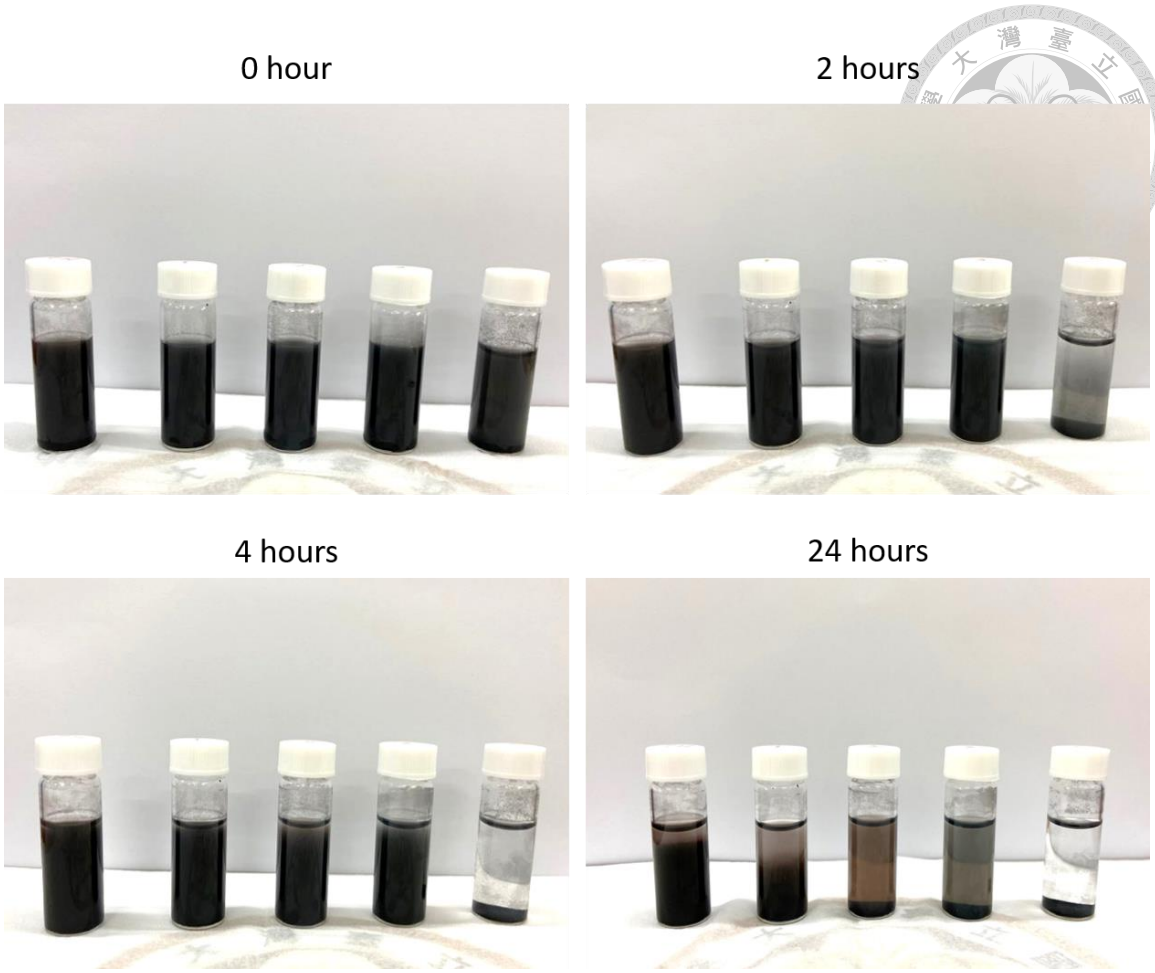

Figure 3-9. 4 wt % of PEDOT-OH and nanocomposites dispersed in DI water. Suspension solutions of PEDOT-OH, 0.3_Ti_2O_3@PEDOT-OH, 0.7_Ti_2O_3@PEDOT-OH, 1.0_Ti_2O_3@PEDOT-OH, and 1.5_Ti_2O_3@PEDOT-OH, respectively, from left to right.

doi:10.6342/NTU202201614

3.2 CAU-10-H Membranes

3.2.1 Surface Morphology and Thickness

In-situ CAU-10-H membranes were well synthesized in this work by secondary and third growth in a reflux condition. The structure of CAU-10-H is shown in **Figure 3-10**. Five CAU-10-H membranes with different thicknesses were fabricated to demonstrate the consequent effects further. In fabrication, the concentration of the secondary-growth solution and the temperature were raised to enhance the thickness of CAU-10-H. And the volume of DMF was simultaneously slightly increased to prevent cosolvent boiling in the synthesis. The morphology and microstructures of all membranes were determined by SEM. A Hitachi S-4800 field emission SEM was used with an acceleration voltage of 10 kV. The SEM results show that a PTFE substrate possesses a loose foam with high porosity, which benefits water absorption applications (**Figure 3-11a, Figure 3-12a**). It also shows that the thickness of a PTFE substrate is about 15 μm (**Figure 3-12a**). According to the SEM images of CAU-10-H membranes, with a lower concentration of reaction solution, the grains of *in-situ* CAU-10-H are slender and flakier (**Figure 3-11b,d**). By comparison, the grains are much coarser synthesized with a higher concentration of the solution (**Figure 3-11c,e,f**). In cross-section SEM results, different thicknesses, 7 μm, 10 μm, 13 μm, 15 μm, and 17 μm CAU-10-H membranes were successfully fabricated (**Figure 3-12b,c,d,e,f**). Contrary to the microstructure of a PTFE substrate, *in-situ* CAU-10-H presents a dense layer, and the intergranular gaps provide paths for water permeation by the capillary force. Moreover, the thickness of CAU-10-H increases because of a higher reaction concentration and temperature (**Figure 3-12c**). Also, in third growth synthesis, replacing reactant solutions provides double the quantity of reactants and reaction time for the

doi:10.6342/NTU202201614

growth of CAU-10-H crystal, making the *in-situ* CAU-10-H layer considerably thicker (**Figure 3-12d,e,f**).

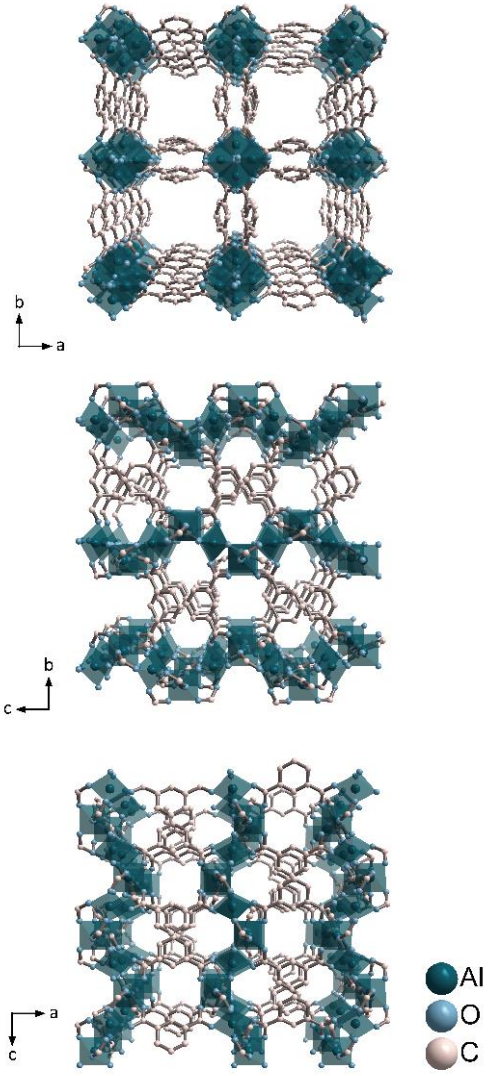

Figure 3-10. Schematic illustration of CAU-10-H structure, where AlO_6 octahedra are green, oxygen atoms are blue, and carbon atoms are light brown.

doi:10.6342/NTU202201614

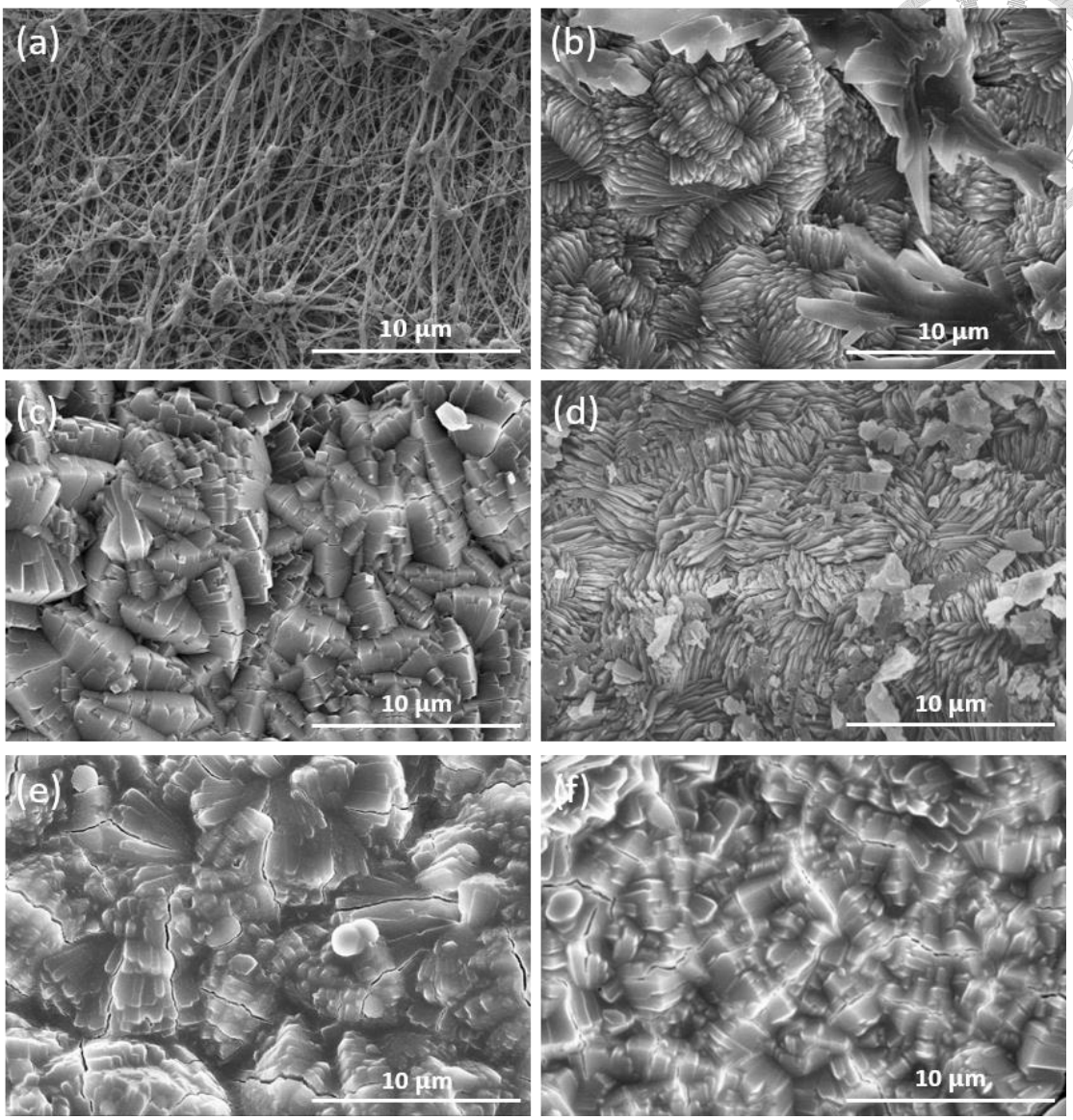

Figure 3-11. SEM results. (a) PTFE substrate. (b) 7 μm thick CAU-10-H. (c) 10 μm thick CAU-10-H. (d) 13 μm thick CAU-10-H. (e) 15 μm thick CAU-10-H. (f) 17 μm thick CAU-10-H. 5000x. Scale bar: 10 μm.

doi:10.6342/NTU202201614

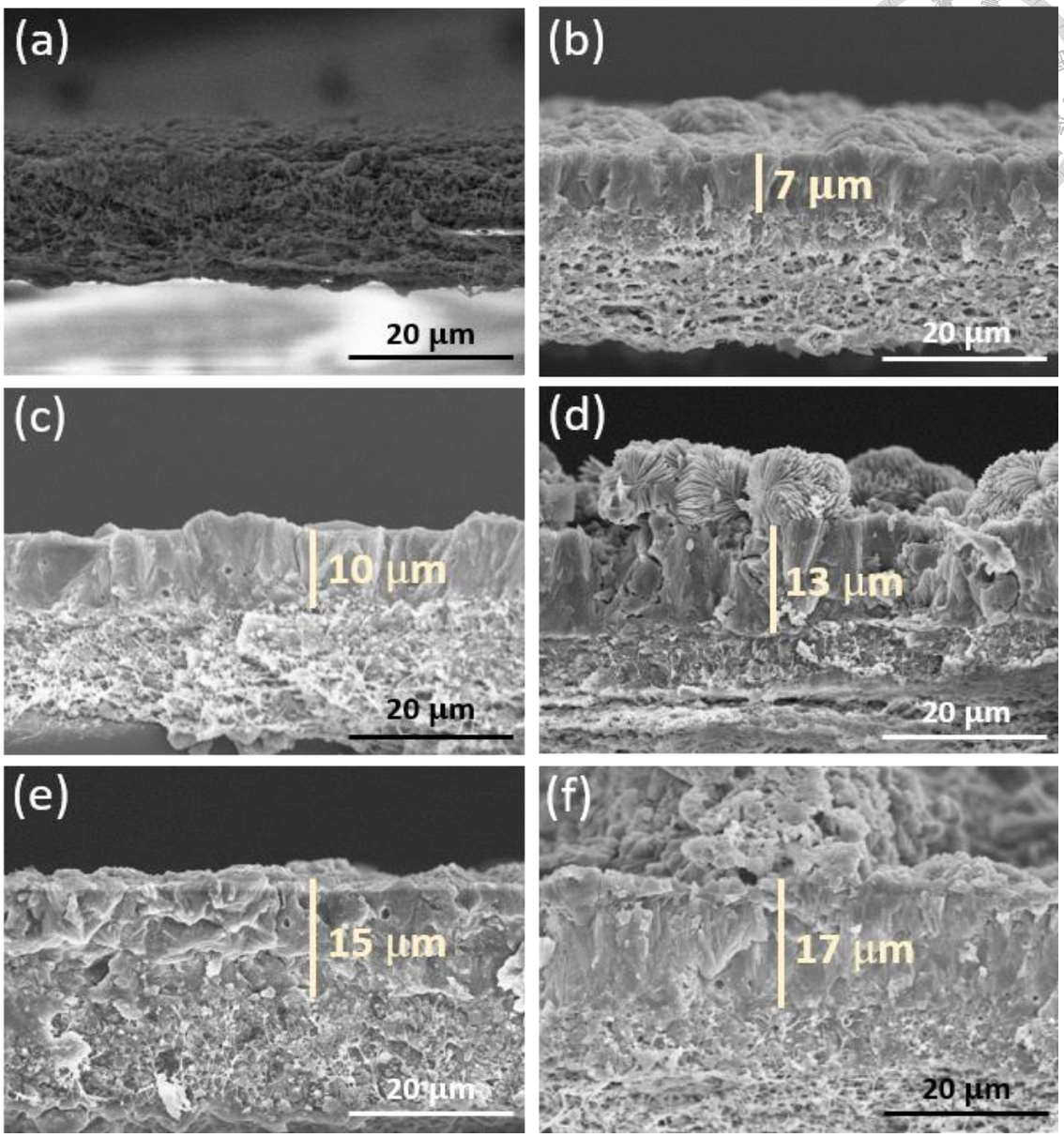

Figure 3-12. Cross-section SEM results. (a) PTFE substrate. (b) 7 μm thick CAU-10-H. (c) 10 μm thick CAU-10-H. (d) 13 μm thick CAU-10-H. (e) 15 μm thick CAU-10-H. (f) 17 μm thick CAU-10-H. 2000x. Scale bar: 20 μm.

doi:10.6342/NTU202201614

To exemplify the necessity of an *in-situ* CAU-10-H layer in the temperature and evaporation tests, a CAU-10-H powder seeded membrane was prepared by repeating the seeding process five times to acquire powder covering the surface. The SEM images of a seeded membrane are shown in **Figure 3-13**. The particles are stuck in PTFE fibrous foam, reducing the pore sizes of the substrate, and distributed uniformly without aggregation (**Figure 3-13a)**. In the cross-section SEM image, the thickness of the seeded membrane remains the same as the PTFE substrate, indicating only a thin layer formed by powder seeding (**Figure 3-13b**).

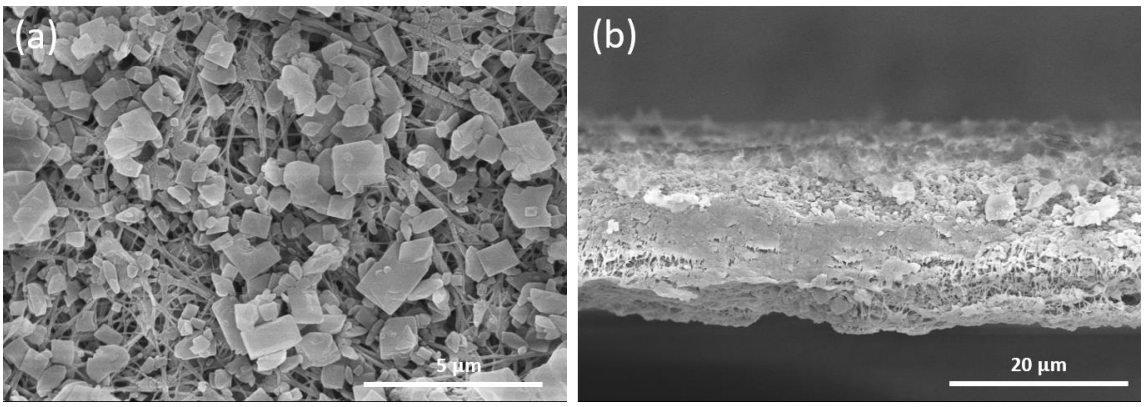

Figure 3-13. SEM results of a seeded membrane (a) Front image. 8000x. Scale bar: 5µm. (b) Cross section. 2000x. Scale bar: 20 µm.

doi:10.6342/NTU202201614

3.2.2 Crystal Analysis

XRD results of CAU-10-H membranes have been demonstrated to exemplify the consistency of crystal structure under different reaction conditions (**Figure 3-14a**). 7 μm CAU-10-H, 10 μm CAU-10-H, and 15 μm CAU-10-H membranes synthesized with different concentrations, temperatures, and ratios of solvents possess the same characteristic peaks in XRD results, which fit the overlap of CAU-10-H simulation and the result of a PTFE substrate. The slight offsets of characteristic peaks between each membrane and the simulation come from different thicknesses and heights. On the other hand, the small peaks at about 12° 2θ and 13.5° 2θ of membranes also fit the peaks at 11.7° 2θ and 13.6° 2θ in the amplified result of CAU-10-H simulation (**Figure 3-14b**). Because of remaining water molecules in porous structure, these actual peaks of membranes are much magnified than the peaks in simulation. Overall, all characteristic peaks in the XRD result show that synthesizing with different concentrations, temperatures, and the ratios of cosolvent does not evidently affect the crystal structure.

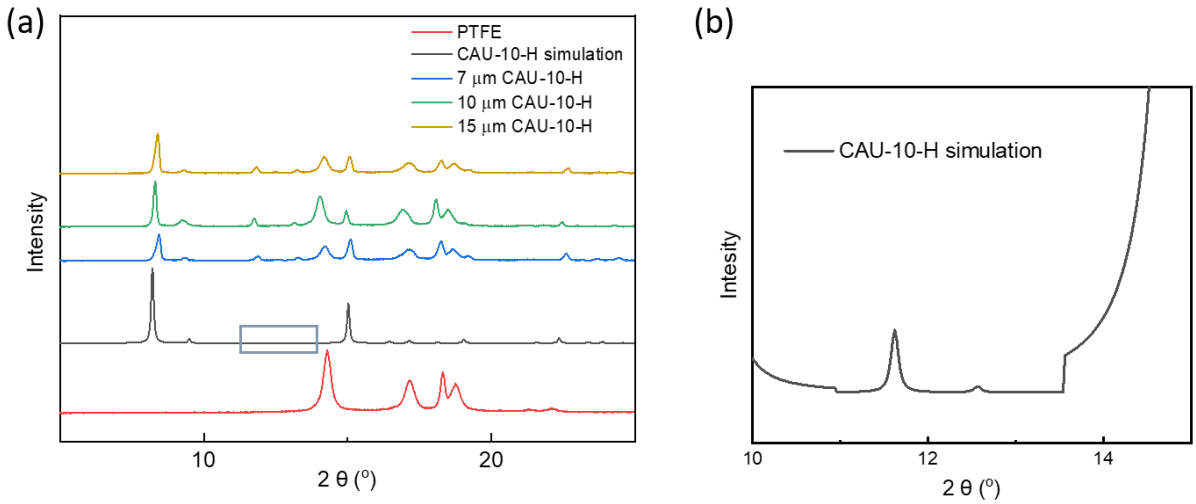

Figure 3-14. (a) XRD results of in-situ CAU-10-H membranes and a PTFE substrate. (b) The magnified region of CAU-10-H simulation in the gray frame in figure (a).

doi:10.6342/NTU202201614

3.3 Surface Analysis of Coating Membranes

3.3.1 Contact Angle

The hydrophilicity of each layer of the membrane is crucial for efficient water absorption, transportation, and the consequent evaporation rate. Functionalized PTFE substrate and EDOT with hydroxymethyl groups were chosen to meet the requirement. To investigate the hydrophilicity, immediate contact angle results were measured (**Figure 3-15a**). A functionalized PTFE substrate possesses a contact angle of 38.89^{o}, much lower than the one of ordinary PTFE. *In-situ* CAU-10-H with a contact angle of 26.05^{o} is comparable hydrophilic to other MOFs and is suitably applied for water evaporation. The contact angle results of different light-absorbing nanocomposites are also presented. Quoteworthy, hydrogen bonds would form between Ti_2O_3 and water molecules, making Ti_2O_3 coating hold a low contact angle of 18.79^{o}. Functionalized PEDOT with hydroxyl side groups possesses a contact angle of 48.38^{o}, much lower than PEDOT, about 110^{o}. With the high hydrophilicity of Ti_2O_3 nanoparticles, Ti_2O_3@PEDOT-OH coating also presents a low contact angle of 24.30^{o}, and its hydrophilicity could be beneficial to be coated on CAU-10-H and improve the evaporation rate. Because of micron and submicron pores in the fibrous foam and particles, water drops on a PTFE substrate, Ti_2O_3 particles, and PEDOT-OH coating in the measurements were absorbed into the samples within a few seconds (**Figure 3-15b**).

doi:10.6342/NTU202201614

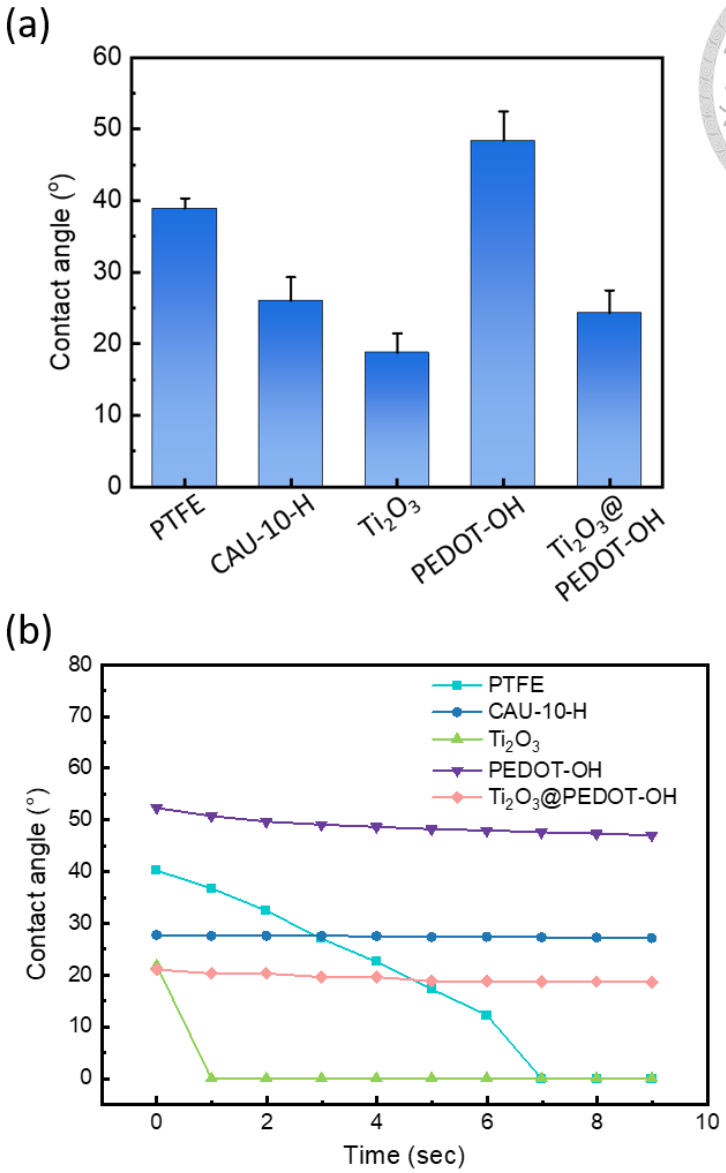

Figure 3-15. (a) Immediate contact angles. (b) Contact angles in ten seconds.

doi:10.6342/NTU202201614

3.3.2 Surface and Cross-Section Morphology

SEM results also demonstrated the morphology of Ti_2O_3@PEDOT-OH on CAU-10-H membranes after coating. The image shows the particle sizes of nanocomposites are about one hundred nanometers and that Ti_2O_3@PEDOT-OH nanocomposites were averagely dispersed without aggregation **(Figure 3-16a**). In the cross-section SEM result, three perfect layers are presented: a PTFE substrate's porous structure for water absorption, a dense *in-situ* CAU-10-H for water permeation, and a Ti_2O_3@PEDOT-OH coating with micropores for light absorption and water evaporation (**Figure 3-16b**).

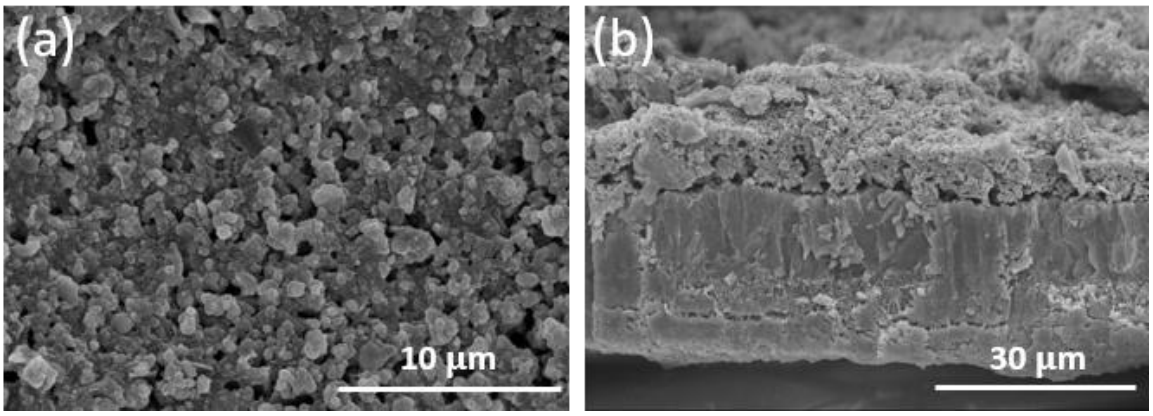

Figure 3-16. SEM results of Ti_2O_3@PEDOT-OH coating on CAU-10-H. (a) The front. 5000x. Scale bar: 10 μm. (b) Cross-section. 1500x. Scale bar: 30 μm.

doi:10.6342/NTU202201614

3.3.3 Device Setup

As Figure 3-2 shows, the evaporation tests were conducted with two different setups, on the 3D printing device and directly floating on bulk water. The evaporation results are shown in **Table 3-2**, **Figure 3-17**. The evaporation rates of *in-situ* CAU-10-H membranes are all elevated directly on water because of the thermal insulation of dense CAU-10-H. Placing membranes on water efficiently raises water absorption and transportation. In the comparison of two setups, the rates enhance more significantly as the thicknesses of CAU-10-H increase, further evidencing that the insulating ability rises with the thickness **Table 3-2**. However, the evaporation rate of the coating PTFE substrate conversely decreases compared to the device setup. It reveals that the substrate lacks thermal insulation without the additional device and CAU-10-H layer. These results demonstrate that the sufficient thermal insulating ability and self-floating ability of *in-situ* CAU-10-H membranes benefit practical steam generation.

Table 3-2. Evaporation rates of 1.0 _ Ti_2O_3@PEDOT-OH nanocomposites coating with two different setups.

	Evaporation rates ($kg \cdot m^{-2} \cdot h^{-1}$)	
	On device	**On water**
On PTFE	1.327	0.925
CAU-10-H powder	1.071	1.095
On 7um_CAU-10-H	1.624	1.690
On 10um_CAU-10-H	1.825	1.891
On 13um_CAU-10-H	1.909	2.294
On 15um CAU-10-H	1.308	1.617

doi:10.6342/NTU202201614

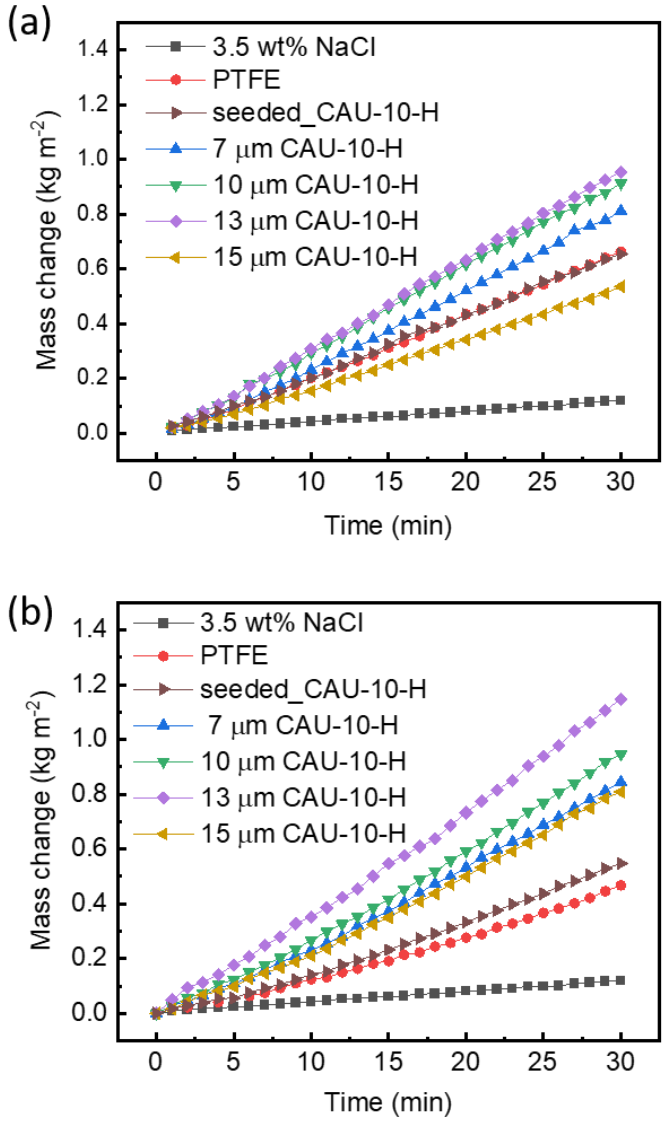

Figure 3-17. Evaporation rates of 1.0 _ Ti_2O_3@PEDOT-OH nanocomposites coating on PTFE substrate, CAU-10-H seeded substrate and CAU-10-H membranes with different thicknesses under one sun illumination. 3.5 wt % NaCl solution was applied in the measurements. (a) On device. (b) On bulk water.

doi:10.6342/NTU202201614

3.4 Solar Desalination Tests

3.4.1 Photothermal Capacity

To further demonstrate the local heat effects of CAU-10-H membranes, the comparison of temperatures in a dry and a wet state has been measured upon one sun illumination. Furthermore, to compare the heat insulating ability between *in-situ* CAU-10-H and CAU-10-H particles, CAU-10-H powder seeded membranes were prepared by repeating the seeding process five times to acquire dense particles to cover the substrate. All membranes were coated with 1.0_ Ti_2O_3@PEDOT-OH. In a dry state, after 10 minutes of illumination, the coated surfaces of a PTFE substrate, particle seeded substrate, 7 μm, 10 μm, 13 μm, 15 μm, and 17 μm CAU-10-H membranes heat up to 71.5 ºC, 73.4 ºC, 76.4 ºC, 79 ºC, 81.9 ºC, 82.1 ºC, and 88.6 ºC, respectively (**Figure 3-18a**, **Figure 3-19**). In a wet-state measurement, all membranes are directly floating on the water without an additional insulator. After 1 hour of illumination, the coated surfaces of a PTFE substrate, particle seeded substrate, 7 μm, 10 μm,13 μm, 15 μm, and 17 μm CAU-10-H membranes heat up to 41.8 ºC, 41.9 ºC, 41.9 ºC, 42.4 ºC, 43.3 ºC, 44.8 ºC, and 45.4 ºC, respectively (**Figure 3-18b**, **Figure 3-20**). It shows that temperature trends are positively related to the thicknesses in both states. The coated 17 μm CAU-10-H possesses the highest temperatures, 17.5 ºC and 3.6 ºC, more elevated than the PTFE substrate without CAU-10-H insulating the heat. Additionally, even though a coated CAU-10-H particle seeded membrane is slightly more heated than a coated PTFE substrate, the temperatures at a wet state are almost the same, presenting that only particle deposition cannot serve as a sufficient heat insulator floating on bulk water. Accordingly, the temperature measurements show that the dense *in-situ* CAU-10-H layer is critical in concentrating heat on the surface.

doi:10.6342/NTU202201614

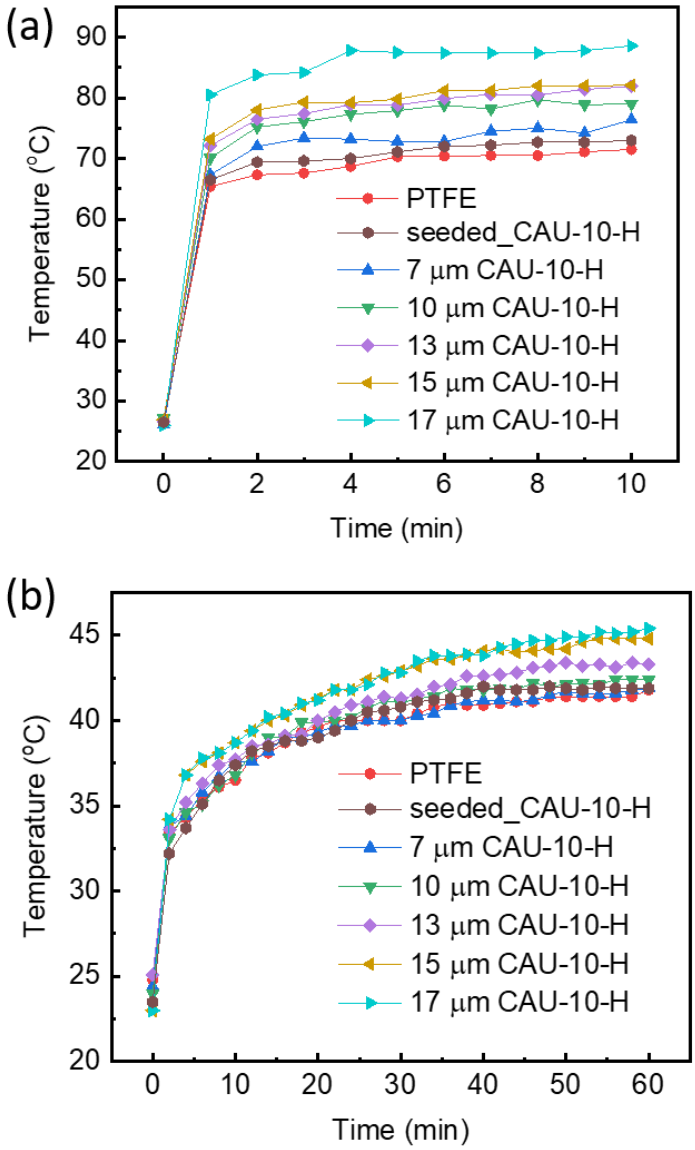

Figure 3-18. (a) Temperatures at a dry state of 1.0 _Ti_2O_3@PEDOT-OH nanocomposites coating on PTFE substrate and CAU-10-H membranes with different thicknesses under one sun illumination. (b) Temperatures at a wet state of 1.0 _ Ti_2O_3@PEDOT-OH nanocomposites coating on PTFE substrate and CAU-10-H membranes with different thicknesses under one sun illumination.

doi:10.6342/NTU202201614

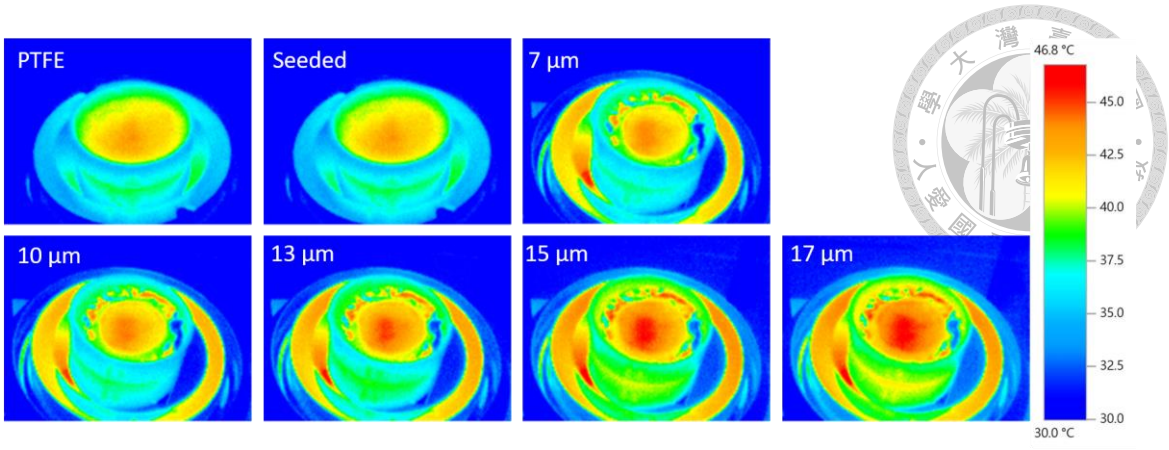

Figure 3-19. IR images of coated PTFE substrate, seeded membrane, and *in-situ* CAU-10-H membranes with different thicknesses in a dry state after ten minutes one-sun irradiation.

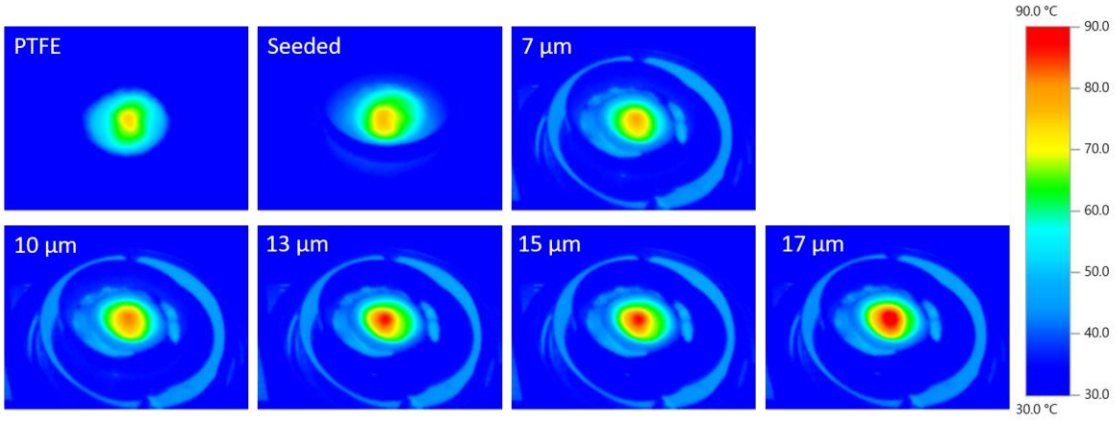

Figure 3-20. IR images of coated PTFE substrate, seeded membrane, and *in-situ* CAU-10-H membranes with different thicknesses in a wet state after thirty minutes one-sun irradiation.

doi:10.6342/NTU202201614

3.4.2 Evaporation Tests

In the ideal device, the heat transformed from solar irradiation should be concentrated on the surface and contribute to water vapor enthalpy. As the thickness of *in-situ* CAU-10-H increases, the dense crystals should prevent the heat which Ti_2O_3@PEDOT-OH absorbs and converts from solar energy conducting through water molecules and heating water beneath the membranes. As a result, the temperature difference between the two sides of membranes would be the largest and benefit steam generation. On the other hand, if the water permeation paths become too long as rising thickness, water molecules would not be able to transport upward efficiently by a capillary force, and the evaporation rate of the device would be eliminated. Thus, the thickness of *in-situ* CAU-10-H is crucial to maintaining the balance of the two mechanisms.

To investigate the solar steam capacity and verify the aforementioned mechanism, the evaporation rate was measured with the samples directly floating on a 3.5 wt % NaCl aqueous solution, simulating seawater. The mass change over time was conducted with the solar simulator and measured by an electronic analytic balance (**Figure 3-21**). The efficiencies of all CAU-10-H membranes are significantly higher than the membranes without *in-situ* CAU-10-H, clearly confirming that the dense crystal layer can confine heat and reduce energy loss to bulk water. The result presents that Ti_2O_3@PEDOT-OH on a 13 μm CAU-10-H membrane possesses the highest evaporation rate of 2.17 $kg \cdot m^{-2} \cdot h^{-1}$. The evaporation rate improves from 7 μm CAU-10-H to 13 μm CAU-10-H due to the heat insulating ability enhanced with increasing thickness. Nevertheless, the evaporation rate drops from 13 μm CAU-10-H to 17 μm CAU-10-H. Although a coated 15 μm and 17 μm CAU-10-H membrane has better solar to thermal conversion capacity because of the heat-insulating ability of

doi:10.6342/NTU202201614

in-situ CAU-10-H, the pathways between dense crystals are too long for efficient water permeation. As a result, the evaporation quantity is limited and declines. Furthermore, Ti_2O_3@PEDOT-OH on a particle seeded membrane as an evaporator possesses a low evaporation rate nearly the same as Ti_2O_3@PEDOT-OH directly coated on a substrate. It indicates that the pores and the unclasp structure in the deposition of particles cannot adequately insulate heat when the membrane is on bulk water without thermal insulators. As a result, compared to Ti_2O_3@PEDOT-OH on the seeded membrane and PTFE substrate, the evaporation rates of membranes with *in-situ* CAU-10-H are significantly higher, evidencing that the appropriate CAU-10-H layer not only confines heat on the surface but also provide efficient permeating paths, further proving that tuning the thickness of CAU-10-H can reach the balance of the two mechanisms.

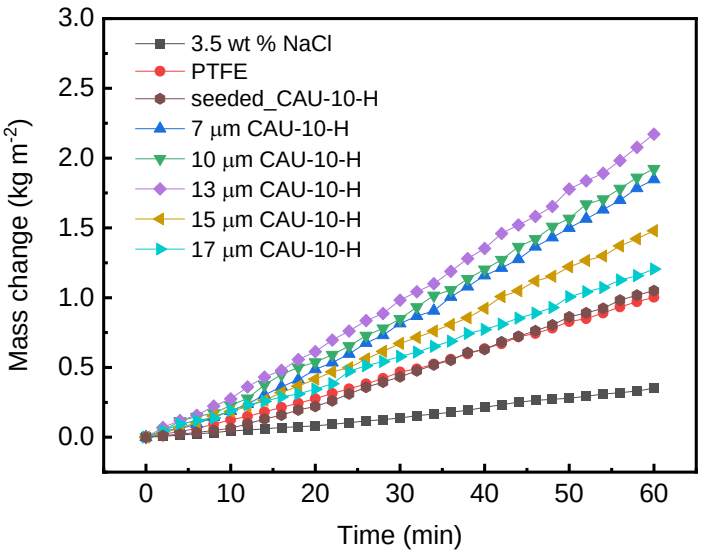

Figure 3-21. Evaporation rates of 1.0_Ti_2O_3@PEDOT-OH nanocomposites coating on PTFE substrate, CAU-10-H seeded substrate, and CAU-10-H membranes with different thicknesses under one sun illumination. 3.5 wt % NaCl aqueous solution was used in the measurements.

The capacity and stability of photothermal conversion of the coating material are

doi:10.6342/NTU202201614

decisive for solar steam generation. To verify the photothermal response of 1.0_Ti_2O_3@PEDOT-OH on 13 μm *in-situ* CAU-10-H, temperature measurements at a dry state were utilized for three illumination cycles (**Figure 3-22a**). Under one sun illumination, the coating surface was sharply heated and reached 86.1 ^oC, 84.4 ^oC, and 86.2 ^oC, respectively, in ten minutes. When simulated solar light was turned off, the temperatures dramatically decreased in the first minute. They fell back to 31.6 ^oC, 31.8 ^oC, and 31.7 ^oC, respectively, slightly above the initial temperature of 27.8 ^oC in 10 minutes. In this measurement, the rapid temperature change reveals the excellent photothermal response capability of Ti_2O_3@PEDOT-OH. Also, the similar performances of the membrane in repetitive irradiation and cooling cycles show its high photothermal stability. To further demonstrate the stability of solar evaporation ability, repetitive evaporation measurements of 1.0_Ti_2O_3@PEDOT-OH on a 13 μm *in-situ* CAU-10-H membrane were conducted under simulated solar light (**Figure 3-22b**). Due to the dense and stable crystal structure of *in-situ* CAU-10-H with excellent mechanical properties, the microstructure of the membrane does not change during the steam generation process. The evaporation rates maintain in five cycles, independent of the repeating cycle, with an average evaporation rate of 2.20 $kg \cdot m^{-2} \cdot h^{-1}$. An evaporation test was conducted again after a month with the same 13 μm *in-situ* CAU-10-H membrane, the evaporation rate maintains at 2.3 $kg \cdot m^{-2} \cdot h^{-1}$. This result demonstrates that coated *in-situ* CAU-10-H is reusable and resistant repeatedly to water desalination.

doi:10.6342/NTU202201614

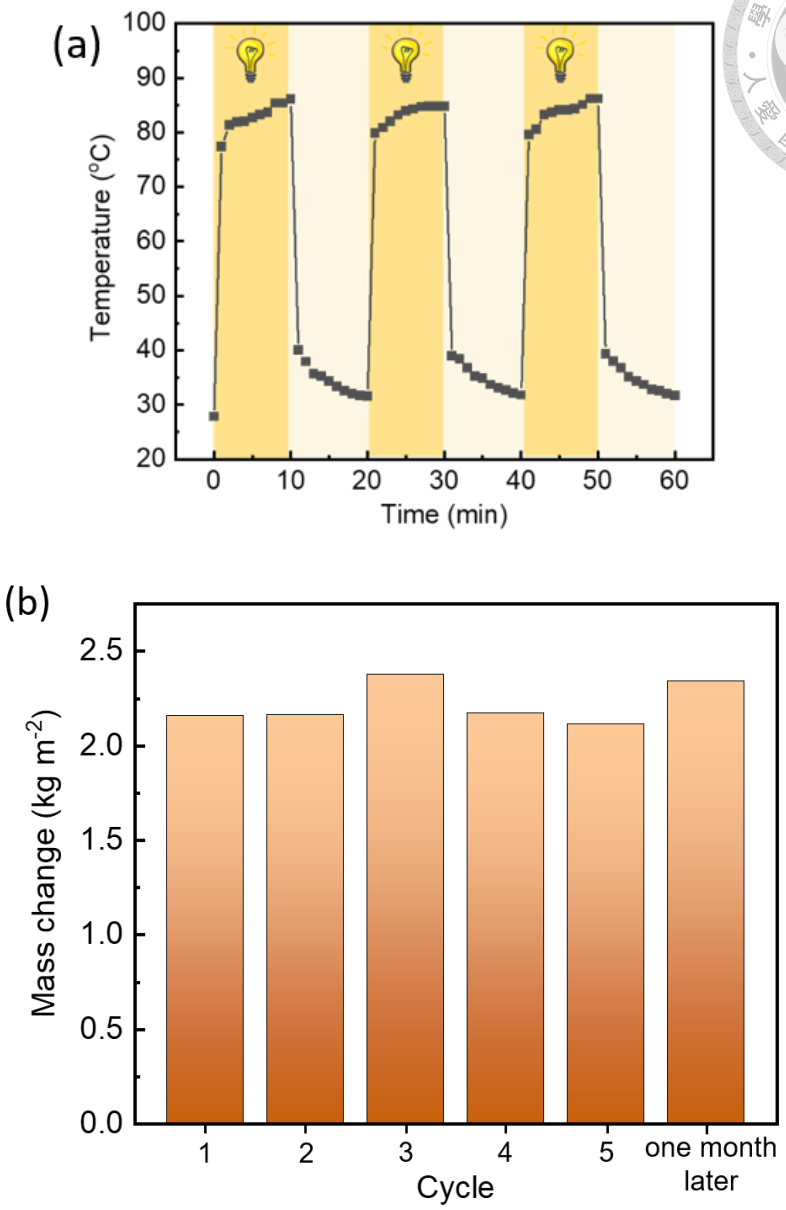

Figure 3-22 (a) Repeat illumination of 1.0_Ti_2O_3@PEDOT-OH nanocomposites coating on 13 μm CAU-10-H membranes at a dry state under one sun illumination. (b) Repeat evaporation rate measurements of 1.0_Ti_2O_3@PEDOT-OH nanocomposites coating on 13 μm CAU-10-H membranes under one sun illumination.

doi:10.6342/NTU202201614

3.4.3 Evaporation Efficiency

To construct the photothermal capacity, the evaporation efficiency of 1.0_Ti_2O_3@PEDOT-OH nanocomposites coating on a 13 μm CAU-10-H membrane has been calculated with **Equation 3-1.** η is evaporation efficiency, $\dot{m}$ is the mass flux of steam that the evaporation rate in a dark condition is subtracted, h_{lv} is the total enthalpy of latent heat which refers to specific heat and latent heat of water vaporization, and I is incident solar radiation density.

$$\eta = \dot{m}h_{lv}/I \qquad \textbf{Equation 3-1.}$$

A coated 13 μm CAU-10-H membrane holds an evaporation rate of 0.77 $kg \cdot m^{-2} \cdot h^{-1}$ in a dark environment. The water vaporization enthalpy at 40.26 ºC, which is the average temperature of membrane surface, is about 2400 $kJ \cdot kg^{-1}$. The solar irradiation density of one-sun illumination is 1 $kW \cdot m^{-2}$. After calculating, a coated 13 μm CAU-10-H membrane possesses an evaporation efficiency of 95.3 %, which refers 95.3% of total irradiation energy converts into the heat absorbed by water to steam escaping. Overall, this result indicates that, even without additional thermal insulators preventing heat loss, the membrane possesses the high photothermal capacity and conversion efficiency.

doi:10.6342/NTU202201614

3.4.4 Practical Application and Purification Analysis

The practical solar desalination of Ti_2O_3@PEDOT-OH on a 13 μm CAU-10-H membrane was conducted with the homemade device (**Figure 3-23**). The aqueous solution was prepared to simulate seawater, and the chemical composition is shown in **Table 3-3.** Simulated seawater was vaporized through the membrane and condensed into pure water in the glass device. 13 μm CAU-10-H membrane coated Ti_2O_3@PEDOT-OH reached an evaporation rate of 1.63 $kg \cdot m^{-2} \cdot h^{-1}$ with the device. Additionally, condensed water was collected and characterized with inductively coupled plasma mass spectrometry (ICP-MS, 7700e, Agilent). Metal ion concentrations are analyzed and compared to those of simulated seawater to reveal the seawater desalination performance (**Figure 3-24**). The ion concentrations of purified water are significantly eliminated by three orders of magnitudes and well qualified with drinkable water standards by WHO. The results evidence that coated CAU-10-H membranes possess the outstanding ability of desalination and can be practically applied as solar desalination membranes and steam generators.

Table 3-3. The ion concentrations of simulated seawater.

Ions	**Concentrations (wt %)**
Na^+	1.12
Mg^{2+}	0.11
Ca^{2+}	0.041
K^+	0.06
SO_4^{2-}	0.032
Cl^-	1.96

doi:10.6342/NTU202201614

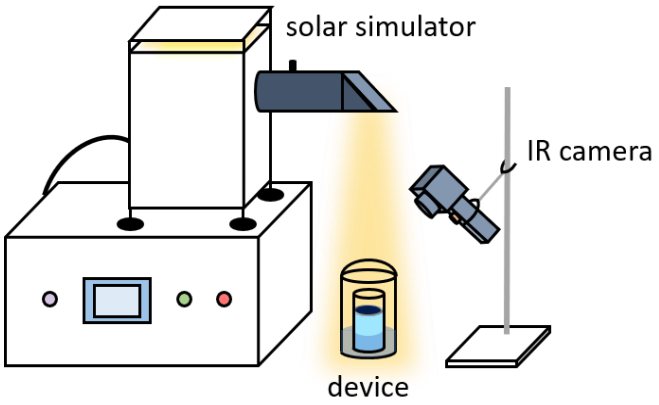

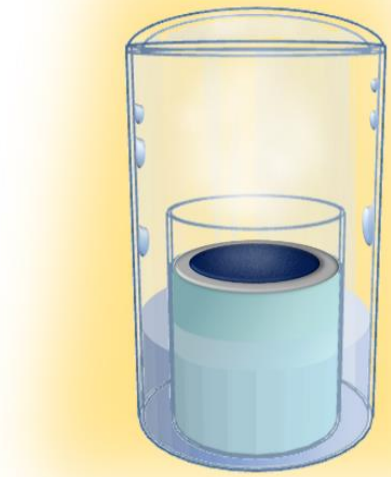

Figure 3-23. Device setup to collect condensed pure water.

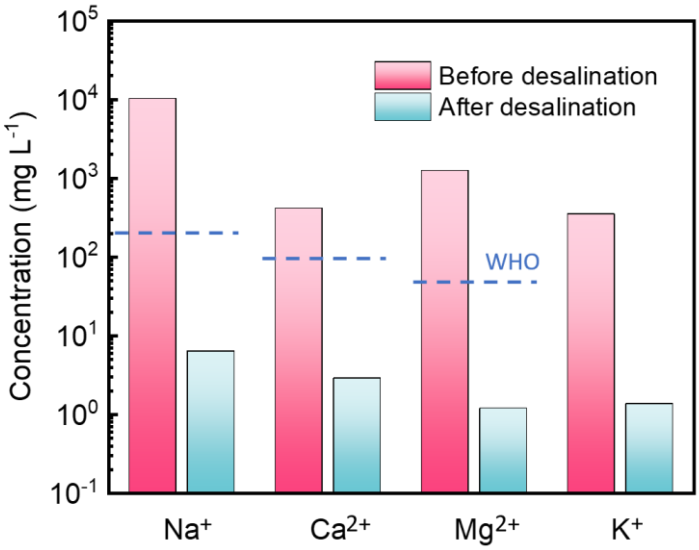

Figure 3-24. Ion concentrations of simulated seawater before and after desalination.

doi:10.6342/NTU202201614

Chapter 4 Conclusion

In summary, we successfully fabricated *in-situ* CAU-10-H membranes coating with nanoTi_2O_3@PEDOT-OH in this work for solar steam generation and desalination. 1.0_nanoTi_2O_3@PEDOT-OH have been demonstrated to be an excellent solar absorber with high light absorption and photothermal capacity for coating. On the other hand, *in-situ* CAU-10-H membranes with high porosity, thermal insulating ability, and low thermal conductivity are manifested as promising desalination membranes with a crystalline structure. Especially, a coated 13 μm thick CAU-10-H membrane possesses the best performance in evaporation tests with efficient thermal insulation and water permeation. 1.0_nanoTi_2O_3@PEDOT-OH coated 13 μm CAU-10-H membranes with self-floating ability reach an average evaporation rate of 2.20 $kg \cdot m^{-2} \cdot h^{-1}$ in five cycles with an efficiency of 95.3% indicating its consistent steam generating capacity. In addition, a practical device has been revealed in this work to desalinate simulated seawater into drinkable water with ion concentrations eliminated by three orders of magnitudes. These results show that Ti_2O_3@PEDOT-OH nanocomposites coating on 13 μm CAU-10-H membranes has excellent potential for future solar steam generation and desalination.

doi:10.6342/NTU202201614

Chapter 5 Future Work

The morphologies of CAU-10-H depend on the concentrations of secondary-growth solutions and might affect water permeation. The effects can be further demonstrated in evaporation tests. Besides, the water-absorbing ability of hydrophilic PTFE substrates can be improved. Also, there is room for modifying the water desalination device to enhance desalination rates and reach the same speeds as evaporation.

doi:10.6342/NTU202201614

REFERENCE

1. Zhu, L., et al., *Solar-driven photothermal nanostructured materials designs and prerequisites for evaporation and catalysis applications.* Materials Horizons, 2018. **5**(3): p. 323-343.
2. Li, Z.T., et al., *Fast-Growing Field of Interfacial Solar Steam Generation: Evolutional Materials, Engineered Architectures, and Synergistic Applications.* Solar Rrl, 2019. **3**(3).
3. Li, Z., et al., *Solar-Powered Sustainable Water Production: State-of-the-Art Technologies for Sunlight–Energy–Water Nexus.* ACS Nano, 2021. **15**(8): p. 12535-12566.
4. Ni, G., et al., *Steam generation under one sun enabled by a floating structure with thermal concentration.* Nature Energy, 2016. **1**(9): p. 16126.
5. Zhao, F., et al., *Materials for solar-powered water evaporation.* Nature Reviews Materials, 2020. **5**(5): p. 388-401.
6. Xiong, Z.-C., et al., *Flexible Fire-Resistant Photothermal Paper Comprising Ultralong Hydroxyapatite Nanowires and Carbon Nanotubes for Solar Energy-Driven Water Purification.* Small, 2018. **14**(50): p. 1803387.
7. Mu, P., et al., *Superwetting Monolithic Hollow-Carbon-Nanotubes Aerogels with Hierarchically Nanoporous Structure for Efficient Solar Steam Generation.* Advanced Energy Materials, 2019. **9**(1): p. 1802158.
8. Wang, Z., et al., *Pathways and challenges for efficient solar-thermal desalination.* Science Advances, 2019. **5**(7): p. eaax0763.
9. Cahill, D.G., et al., *Nanoscale thermal transport. II. 2003–2012.* Applied Physics Reviews, 2014. **1**(1): p. 011305.
10. Han, S., et al., *Cellulose-Conducting Polymer Aerogels for Efficient Solar Steam Generation.* Advanced Sustainable Systems, 2020. **4**(7): p. 2000004.
11. Salehi, A.A., et al., *Hydrogel materials as an emerging platform for desalination and the production of purified water.* Separation and Purification Reviews, 2021. **50**(4): p. 380-399.
12. Zhou, X.Y., et al., *Topology-Controlled Hydration of Polymer Network in Hydrogels for Solar-Driven Wastewater Treatment.* Advanced Materials, 2020.

doi:10.6342/NTU202201614

32(52).

13. Zhao, F., et al., *Highly efficient solar vapour generation via hierarchically nanostructured gels.* Nature Nanotechnology, 2018. **13**(6): p. 489-+.
14. Zhou, X.Y., et al., *Architecting highly hydratable polymer networks to tune the water state for solar water purification.* Science Advances, 2019. **5**(6).
15. Zhou, X.Y., et al., *A hydrogel-based antifouling solar evaporator for highly efficient water desalination.* Energy & Environmental Science, 2018. **11**(8): p. 1985-1992.
16. Guo, Y.H., et al., *Synergistic Energy Nanoconfinement and Water Activation in Hydrogels for Efficient Solar Water Desalination.* Acs Nano, 2019. **13**(7): p. 7913-7919.
17. Lu, Y., et al., *Turning Trash into Treasure: Pencil Waste-Derived Materials for Solar-Powered Water Evaporation.* Energy Technology, 2020. **8**(10).
18. Zhao, F., et al., *Materials for solar-powered water evaporation.* Nature Reviews Materials, 2020. **5**(5): p. 388-401.
19. Zhao, X., et al., *Janus Polypyrrole Nanobelt@Polyvinyl Alcohol Hydrogel Evaporator for Robust Solar-Thermal Seawater Desalination and Sewage Purification.* Acs Applied Materials & Interfaces, 2021. **13**(39): p. 46717-46726.
20. Xu, W.Z., et al., *Efficient Water Transport and Solar Steam Generation via Radially, Hierarchically Structured Aerogels.* Acs Nano, 2019. **13**(7): p. 7930-7938.
21. Hu, X.Z., et al., *Tailoring Graphene Oxide-Based Aerogels for Efficient Solar Steam Generation under One Sun.* Advanced Materials, 2017. **29**(5).
22. Zhao, L.Y., et al., *A novel composite hydrogel for solar evaporation enhancement at air-water interface.* Science of the Total Environment, 2019. **668**: p. 153-160.
23. He, J.X., et al., *Fe3O4/PPy-Coated Superhydrophilic Polymer Porous Foam: A Double Layered Photothermal Material with a Synergistic Light-to-Thermal Conversion Effect toward Desalination.* Langmuir, 2021. **37**(42): p. 12397-12408.
24. Zhang, M.R., et al., *Antibacterial evaporator based on reduced graphene oxide/polypyrrole aerogel for solar-driven desalination.* Nano Research, 2022.
25. Dong, X.Y., et al., *Reed Leaves Inspired Silica Nanofibrous Aerogels with*

doi:10.6342/NTU202201614

Parallel-Arranged Vessels for Salt-Resistant Solar Desalination. Acs Nano, 2021. **15**(7): p. 12256-12266.

26. Zheng, Z.H., et al., *Polyimide/MXene hybrid aerogel-based phase-change composites for solar-driven seawater desalination.* Chemical Engineering Journal, 2022. **440**.
27. Zhang, Q., et al., *Flexible and Mildew-Resistant Wood-Derived Aerogel for Stable and Efficient Solar Desalination.* Acs Applied Materials & Interfaces, 2020. **12**(25): p. 28179-28187.
28. Ma, S., et al., *Metal-organic framework derived porous carbon of light trapping structures for efficient solar steam generation.* Solar Energy Materials and Solar Cells, 2019. **196**: p. 36-42.
29. Marco-Lozar, J.P., et al., *MOF-5 and activated carbons as adsorbents for gas storage.* International Journal of Hydrogen Energy, 2012. **37**(3): p. 2370-2381.
30. Li, H., et al., *Porous metal-organic frameworks for gas storage and separation: Status and challenges.* EnergyChem, 2019. **1**(1): p. 100006.
31. Kunowsky, M., F. Suárez-García, and Á. Linares-Solano, *Adsorbent density impact on gas storage capacities.* Microporous and Mesoporous Materials, 2013. **173**: p. 47-52.
32. Mahmoud, E., et al., *Implementing Metal-Organic Frameworks for Natural Gas Storage.* Crystals, 2019. **9**(8): p. 406.
33. Mileo, P.G.M., et al., *Molecular simulation of natural gas storage in Cu-BTC metal–organic framework.* Colloids and Surfaces A: Physicochemical and Engineering Aspects, 2014. **462**: p. 194-201.
34. Li, B., et al., *Nanospace within metal–organic frameworks for gas storage and separation.* Materials Today Nano, 2018. **2**: p. 21-49.
35. Altintas, C., et al., *Machine Learning Meets with Metal Organic Frameworks for Gas Storage and Separation.* Journal of Chemical Information and Modeling, 2021. **61**(5): p. 2131-2146.
36. Xiang, F., A.M. Marti, and D.P. Hopkinson, *Layer-by-layer assembled polymer/MOF membrane for H2/CO2 separation.* Journal of Membrane Science, 2018. **556**: p. 146-153.
37. Stolar, T., et al., *Scalable Mechanochemical Amorphization of Bimetallic Cu−Zn MOF-74 Catalyst for Selective CO2 Reduction Reaction to Methanol.* ACS

doi:10.6342/NTU202201614

Applied Materials & Interfaces, 2021. **13**(2): p. 3070-3077.

38. Chiou, D.-S., et al., *Highly CO2 Selective Metal–Organic Framework Membranes with Favorable Coulombic Effect.* Advanced Functional Materials, 2021. **31**(4): p. 2006924.
39. Qasem, N.A.A., R. Ben-Mansour, and M.A. Habib, *An efficient CO2 adsorptive storage using MOF-5 and MOF-177.* Applied Energy, 2018. **210**: p. 317-326.
40. Lo, Y. and D.-Y. Kang, *Pseudopolymorphic seeding for the rational synthesis of hybrid membranes with a zeolitic imidazolate framework for enhanced molecular separation performance.* Journal of Materials Chemistry A, 2016. **4**(11): p. 4172-4179.
41. Kan, M.-Y., et al., *Activation-Controlled Structure Deformation of Pillared-Bilayer Metal–Organic Framework Membranes for Gas Separations.* Chemistry of Materials, 2019. **31**(18): p. 7666-7677.
42. Ting, H., et al., *High-permeance metal–organic framework-based membrane adsorber for the removal of dye molecules in aqueous phase.* Environmental Science: Nano, 2017. **4**(11): p. 2205-2214.
43. Jabbari, V., et al., *Green synthesis of magnetic MOF@GO and MOF@CNT hybrid nanocomposites with high adsorption capacity towards organic pollutants.* Chemical Engineering Journal, 2016. **304**: p. 774-783.
44. Ding, S., et al., *Targeted degradation of dimethyl phthalate by activating persulfate using molecularly imprinted Fe-MOF-74.* Chemosphere, 2021. **270**: p. 128620.
45. Liu, J., Y. Li, and Z. Lou, *Recent Advancements in MOF/Biomass and Bio-MOF Multifunctional Materials: A Review.* Sustainability, 2022. **14**(10): p. 5768.
46. Yang, W., et al., *Facile fabrication of robust MOF membranes on cloth via a CMC macromolecule bridge for highly efficient Pb(II) removal.* Chemical Engineering Journal, 2018. **339**: p. 230-239.
47. Rego, R.M., et al., *Cerium based UiO-66 MOF as a multipollutant adsorbent for universal water purification.* Journal of Hazardous Materials, 2021. **416**: p. 125941.
48. Rego, R.M., et al., *MOF based engineered materials in water remediation: Recent trends.* Journal of Hazardous Materials, 2021. **403**: p. 123605.
49. Ahsan, M.A., et al., *Sustainable synthesis and remarkable adsorption capacity*

doi:10.6342/NTU202201614

of MOF/graphene oxide and MOF/CNT based hybrid nanocomposites for the removal of Bisphenol A from water. Science of The Total Environment, 2019. **673**: p. 306-317.

50. Chen, Y.-R., T. Tsuru, and D.-Y. Kang, *Simulation and design of catalytic membrane reactor for hydrogen production via methylcyclohexane dehydrogenation.* International Journal of Hydrogen Energy, 2017. **42**(42): p. 26296-26307.
51. Leo, P., et al., *Direct α-arylation of ketones efficiently catalyzed by Cu-MOF-74.* Catalysis Today, 2020. **345**: p. 251-257.
52. Hong, D.H., et al., *MOF-on-MOF Architectures: Applications in Separation, Catalysis, and Sensing.* Bulletin of the Korean Chemical Society, 2021. **42**(7): p. 956-969.
53. Zhang, M., et al., *Chemical Vapor Deposition of Pd(C3H5)(C5H5) to Synthesize Pd@MOF-5 Catalysts for Suzuki Coupling Reaction.* Catalysis Letters, 2012. **142**(3): p. 313-318.
54. Han, X., et al., *Intensifying Heat Using MOF-Isolated Graphene for Solar-Driven Seawater Desalination at 98% Solar-to-Thermal Efficiency.* Advanced Functional Materials, 2021. **31**(13): p. 2008904.
55. Chen, G., et al., *Cu-based MOF-derived porous carbon with highly efficient photothermal conversion performance for solar steam evaporation.* Journal of Materials Chemistry A, 2021. **9**(31): p. 16805-16813.
56. Li, Z., et al., *Polyaniline-Coated MOFs Nanorod Arrays for Efficient Evaporation-Driven Electricity Generation and Solar Steam Desalination.* Advanced Science, 2021. **8**(7): p. 2004552.
57. Ma, Q., et al., *MOF-Based Hierarchical Structures for Solar-Thermal Clean Water Production.* Advanced Materials, 2019. **31**(17): p. 1808249.
58. Wang, J., et al., *A salt-free superhydrophilic metal-organic framework photothermal textile for portable and efficient solar evaporator.* Solar Energy Materials and Solar Cells, 2021. **231**: p. 111329.
59. Le, T.H., Y. Kim, and H. Yoon, *Electrical and Electrochemical Properties of Conducting Polymers.* Polymers, 2017. **9**(4).
60. Nezakati, T., et al., *Conductive Polymers: Opportunities and Challenges in Biomedical Applications.* Chemical Reviews, 2018. **118**(14): p. 6766-6843.

doi:10.6342/NTU202201614

61. Wang, Y., et al., *A highly stretchable, transparent, and conductive polymer.* Science Advances, 2017. **3**(3).
62. Nyholm, L., et al., *Toward Flexible Polymer and Paper-Based Energy Storage Devices.* Advanced Materials, 2011. **23**(33): p. 3751-3769.
63. Zhao, Q.B., et al., *Photothermal converting polypyrrole/polyurethane composite foams for effective solar desalination.* Desalination, 2022. **527**.
64. Sharma, N., et al., *Efficient solar steam generator using black SnOx cored PANI polymeric mesh under one Sun illumination.* Journal of Industrial and Engineering Chemistry, 2022. **107**: p. 45-52.
65. Peng, Y.B., et al., *Bio-inspired vertically aligned polyaniline nanofiber layers enabling extremely high-efficiency solar membrane distillation for water purification.* Journal of Materials Chemistry A, 2021. **9**(17): p. 10678-10684.
66. Zhang, Y.X., et al., *Guaranteeing Complete Salt Rejection by Channeling Saline Water through Fluidic Photothermal Structure toward Synergistic Zero Energy Clean Water Production and In Situ Energy Generation.* Acs Energy Letters, 2020. **5**(11): p. 3397-3404.
67. Li, S., et al., *Cellulose Nanofibril-Stabilized Pickering Emulsion and In Situ Polymerization Lead to Hybrid Aerogel for High-Efficiency Solar Steam Generation.* Acs Applied Polymer Materials, 2020. **2**(11): p. 4581-4591.
68. Zou, Y., et al., *Flexible and Robust Polyaniline Composites for Highly Efficient and Durable Solar Desalination.* Acs Applied Energy Materials, 2020. **3**(3): p. 2634-2642.
69. Yin, X.Y., et al., *Macroporous Double-Network Hydrogel for High-Efficiency Solar Steam Generation Under 1 sun Illumination.* Acs Applied Materials & Interfaces, 2018. **10**(13): p. 10998-11007.
70. Baig, U. and A. Waheed, *Fabrication of polypyrrole-graphitic carbon nitride nanocomposite containing hyper-cross-linked polyamide photoresponsive membrane with self-cleaning properties for water decontamination and desalination applications.* Journal of Water Process Engineering, 2022. **47**.
71. Li, M., et al., *Polymer-decorated daikon-based solar evaporators for efficient interfacial water evaporation.* International Journal of Energy Research, 2022.
72. Sun, Y., et al., *Porous biomass foam of polypyrrole-coated cattail fibers for efficient photothermal evaporation.* Industrial Crops and Products, 2022. **178**.

doi:10.6342/NTU202201614

73. Wang, J.P., et al., *In situ polymerized Fe2O3@PPy/chitosan hydrogels as a hydratable skeleton for solar-driven evaporation.* Journal of the American Ceramic Society, 2022. **105**(8): p. 5325-5335.
74. Wu, M.M., et al., *PPy nanotubes-enabled in-situ heating nanofibrous composite membrane for solar-driven membrane distillation.* Separation and Purification Technology, 2022. **281**.
75. Peng, Y.J., et al., *A High Strength Hydrogel with a Core-Shell Structure Simultaneously Serving as Strain Sensor and Solar Water Evaporator.* Macromolecular Materials and Engineering, 2021. **306**(10).
76. Liu, C.K., et al., *Enhancing solar desalination performance based on restricted salt ions transport.* Journal of Environmental Chemical Engineering, 2021. **9**(4).
77. Zhao, X.Z. and C.K. Liu, *Overcoming salt crystallization with ionic hydrogel for accelerating solar evaporation.* Desalination, 2020. **482**.
78. Han, S.B., et al., *Cellulose-Conducting Polymer Aerogels for Efficient Solar Steam Generation.* Advanced Sustainable Systems, 2020. **4**(7).
79. Liu, C.K., C.J. Cai, and X.Z. Zhao, *Overcoming Salt Crystallization During Solar Desalination Based on Diatomite-Regulated Water Supply.* Acs Sustainable Chemistry & Engineering, 2020. **8**(3): p. 1548-1554.
80. Bi, D.G., et al., *Preparation and characterizations of flexible photothermal Ti2O3-PVA nanocomposites.* Journal of Alloys and Compounds, 2020. **825**.

doi:10.6342/NTU202201614